# An Investigation into Dual-mode Lasing Response in planar multi-layer Plasmonic laser Systems

## Course No.: EEE-400

**Submitted By-**

Shahed-E-Zumrat
Student ID: 1506097

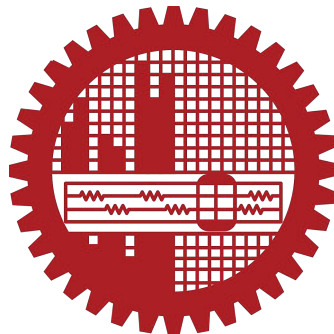Shadman Shahid
Student ID: 1506179

**Submitted To-**

Department of Electrical and Electronic Engineering

*in partial fulfillment of the requirements for the degree of Bachelor of Science in Electrical and Electronic Engineering.*

**Supervised by-**

Dr. Muhammad Anisuzzaman Talukder
Professor
Department of Electrical and Electronic Engineering

Bangladesh University of Engineering and Technology (BUET)
Dhaka-1000, Bangladesh
February, 2021

# Declaration of Authorship

We declare that this thesis titled **"An Investigation into Dual-mode Lasing Response in planar multi-layer Plasmonic laser Systems"** has been written by us, Shahed-E-Zumrat and Shadman Shahid under the supervision of Professor Dr. Muhammad Anisuzzaman Talukder of the Department of Electrical and Electronic Engineering, Bangladesh University of Engineering and Technology (BUET). We would also like to declare the following

- This thesis has been written only to fulfill a requirement for the award of the Bachelor of Science in Electrical and Electronic Engineering degree

- Unless otherwise stated and referred, all contents of this document have been written by the authors

- All external sources have been appropriately attributed

Authors

Shahed-E-Zumrat                                                    Shadman Shahid

Signature of the Supervisor

Dr. Muhammad Anisuzzaman Talukder

Professor
Department of Electrical and Electronic Engineering
Bangladesh University of Engineering and Technology (BUET)

# Acknowledgments

It gives us immense pleasure to have completed our thesis on the aforementioned topic. To begin, our sincerest gratitude goes to Almighty Allah for keeping us in good health and shape to have been able to conduct research properly for the completion of this manuscript. Thereafter, the guidance and support offered by our supervisor Dr. Md. Anisuzzaman Talukder really pushed us forward in continuing our work with endeavour and perseverance. His structured approach and able supervision has instilled in us the proper mindset and approach for conducting an investigative research. His supervision has not only helped us to complete this thesis, but also given us an impetus to solve novel challenges. All throughout our timeline he kept us working up to our full potential and has always been there for us when we required help from him.

While working through this, we received help and encouragement from our fellow classmates, Anik Mazumder, Mozammel and Emon. They have helped us in our work whenever we needed suggestion or technical education. Our esteemed senior and teacher, Zabir Ahmed had been very helpful and provided us assistance our time of need.

The journey in writing this thesis has been a productive learning curve that has taught us quite a lot. However, it would be unfair to not owe our sincere apology to everyone whom we bothered while working for this thesis. How, our friends and family have been patient with us through the up and down journey of this thesis. They have not only tolerated us, but given us strength and encouragement in times of our need.

# Abstract

Miniature lasers emitting dual modes have multifarious applications. However, having dual modes originated from a plasmonic-photonic hybrid has gained research interest only recently. The plasmonic resonance at the junction of a metal nano-hole-array (NHA) and a 1D Photonic Crystal (PhC), known as Tamm states, have been utilized for producing good plasmonic lasing. These single mode lasers posses ultrasmall mode confinement, high modulation speeds and good far-field directionality. Unlike single mode plasmonic lasers, dual mode plasmonic lasers have got attention only very recently, which has lead to ample scope for advancement. The modal volume of plasmonic dual mode lasers that have been reported so far can't necessarily be said to be have been nanoscale. Two planar multi-layer plasmonic laser systems have been reported. In the first design, we report dual mode plasmonic lasing by merging periodicity of the holes to generate a complex periodic metal nano-hole array on top of a 1D Photonic Crystal. Each of the two metal nano-hole array, whose periods were merged, produced isolated singular lasing modes. Both modes support lasing when gain medium is incorporated in the resonator. The motivation of the design came from manipulating and exploring existing resonator designs and observing how design parameters affected the spectral characteristics. By some simple and intuitive design manipulations of the metal nano-hole array, we have been been able to demonstrate dual mode lasing. This finding holds much potential in the field of dual mode nanolasing.

In the second design, the properties distributed Bragg reflectors - DBRs and thin metal nanohole arrays (NHA) come together to create a hybrid dual mode plasmonic lasers. A Linear Asymmetric DBR pair plasmonic laser is reported. It is seen to offer good integration density, lower power, faster response and better confinement of plasmonic lasers along with the lower loss and threshold of semicondutor DBR lasers. This work shows a Tamm plasmon polariton (TPP) - optical Tamm state (OTS) hybrid dual mode laser. The structure incorporates non-plasmonic OTS along with TPP to generate dual mode lasing. The device shows high emission output with extremely narrow linewidth along with a clear and tunable mode separation.

**Keywords**: Plasmonics, Tamm Plasmons, Optical Tamm State, Extarordinary Optical Transmission, Laser, Photonic Crystal,

# Table of Contents

# List of Tables

# List of Figures

# Chapter 1

# Introduction

In the olden days when laser technology was still at its infancy, it used to be said that laser was a solution looking for a problem.[4] Since the invention of this technology and its eventual popularization, it has evolved over the years into an tool indispensable in various fields. As new innovation created new scope, existing technologies have evolved to fill the need. In the field of nanotechnology and nano-electronics, through continuous progress we have been replicating the macroscopic tools in the nano- realm. Following that path, manipulation of coherent radiation in nano scale has bolstered the research in the field of nanophotonic devices and photonic ICs in recent years. Despite its wondrous payoffs nanotechnology comes with its own set of challenges.

## 1.1   Laser Technology and Dual-Mode lasing

Laser (Light Amplification by Stimulated Emission of Radiation) is a form of coherent luminescence due to stimulated electronic transition. The stimulus that forces the electrons to change energy levels is either provided by an optical pump input or by an electrical input (such as an applied electric field or voltage bias). The process of amplification is also termed as 'gain' or 'negative absorption', as per observation.[5] An analysis of the acronym - Light Amplification for Stimulated Emission of Radiation, the incident radiation is the stimulation that causes the gain. The discovery and research into the concepts that led to the refinement of laser as it stands today began at around the 1920's. Einstein's derivation of Planck's discrete energy state formula is essential to the core concept of stimulated emission. Otherwise, the quantum state formula doesn't hold. Initially this phenomenon of 'gain' was termed as 'negative absorption'.[6] Negative absorption, lead to selective anomalous dispersion.[7] The transition of electrons resulted in one of the three processes. For absorbing photon energy an electron would be transferred from a lower energy state to a higher energy state. For emitting photons, electron transition from higher energy state to lower energy state. This emission process could either take place spontaneously without the aid of photon energy. Or, the process could be stimulated by a photon having energy equal to the energy

Figure 1.1: A simplified depiction of a laser system.

difference between the two energy levels where the electron transition takes place. In this scenario while going from higher to lower energy state, the electron emits photon having same phase and energy of the stimulating photon.[8] The stimulant having an energy equal to downward transition energy of electron can be applied by a cavity feedback, with a resonant mode at same energy. This is the usual case in a laser system, as shown in Fig. 1.1. Or the stimulant may be externally provided by a probe pulse of same energy, as seen in pump-probe analyses. This basic principle is utilized in most lasers with slight modifications based upon individual configurations. Lasing is ensured when the higher energy state has more electrons than the lower energy state. This phenomenon, known as population inversion is necessary for lasing to occur. Early lasers incorporated a two-level systems, where emission and absorption of electrons both would take place between two energy levels. The ammonia maser by Townes et. al incorporated a two level laser system.[9] The issue with this configuration was that, the stimulating beam might have ended up getting absorbed by electrons and making them go from lower to higher energy state. The emission eventually dies out, as it cannot sustain population inversion. To better deal with this issue, three level and four level lasers were built. In them, absorption and stimulated emission occur at different wavelengths. Modern systems utilize the four level two electron model.[1] This model better maintains sustained population inversion. Over the years various materials of different phases have been found to generate lasing as 'gain' mediums. They can be a gas or semiconductor or dye embedded in a host medium. Even though the gain medium is the principal part of a laser as shown in Fig. 1.1, it is not the only component that is present in a working laser.

### 1.1.1 Dual-Mode Lasing

Lasers, can emit coherent beams in one or more than one temporal modes, i.e concentration of intensity in distinct frequencies. Dual-mode lasers have ample scope of application, alongside the more explored single mode counterpart. Lasers that emit multiple distinct modes are essential for various applications, including sensing multiple target substances simultaneously,[10,11] distance measurements using two-wavelength interferometry,[12,13] terahertz difference signal generation in microwave communications[14,15] and most importantly in wavelength division multiplexing (WDM) for 'on-chip' optical interconnects (OIs).[16–21] A coherent source emitting at dual wavelengths is especially handy, when such space and design constraints are to be met. Solid-state and semiconductor lasers that can emit multiple modes have been significantly explored. However, it is a great challenge to operate these devices at room temperature as semiconductor gain is highly temperature-dependent. The increase in non-radiative recombination at room temperature reduces optical gain.

## 1.2    Nanophotonics: An introduction to Plasmonics

Coherent light sources with sub-wavelength dimensions have fundamental application and applied significance. Miniaturization of these devices leads to improvement. As technology is advancing, it is reaching the saturation and impeding further miniaturization without decreasing performance. A way out from this situation is believed by replacing electronic devices with optical counterparts[22] or integrating electronic and photonic circuits to get benefit from both the robustness of electronic circuit and bandwidth of optics.[23] For implementing optical fiber based communication, integration of optical and electronic circuits is needed for improvement of performance. But as optical devices are diffraction limited , they are in micrometer range, rather bulky compared to their electronic counterparts which are measured in nanometer range. However, diffraction occurs in EM waves, when they are confined to spatial modes less than half its wavelength. This is the diffraction limit of light. The motivation for nanoscale manipulation of light has led to the enrichment of nano-photonics using <u>plasmonics</u>. Focusing radiation to ranges smaller than the wavelength, (in the nano-meter scale) requires special processes which are not possible in the macroscopic regime. The payoffs of achieving such advancement are multifarious. The dimensional barriers in laser designs are often overcome using the concept of plasmonics. <u>Plasmonics</u> is associated with the manipulation and properties of plasma oscillations. Plasma is the free conduction electrons which are available in abundance in metals. It is these conduction electrons which hold the key to confine electromagnetic radiation beyond diffraction limit. This is primarily contributed to the effects of plasma (hence the term plasm-onics) within a metal. The plasma will show novel properties which can be exploited to be used in nanoscale dimensions.

The lasers miniaturized with plasmonics are potential candidates for applications in sensing and spectroscopy,[24–27] efficient optical interconnects,[28–31] nanolithography,[32–34] super-resolution imaging,[35] biomedical imaging, interconnection between optical and microelectronic devices, detection of nanoscale biomolecules,[36,37] semiconductor transistors. Apart from their use in conjunction with electronic circuits, smaller confinement of light has lot of potential applications. Smaller photo-detectors have lower noise, higher power density and lower operating voltage. Nano-scale lasers can be utilized to store data, create ultra high resolution images for nano-imprinting and as optical interconnects. Such advancement has led to better fabrication technology due to nanolithography along with smaller ICs and interconnects in optoelectronic applications.[30] The ongoing research on third generation solar cells, leveraging higher intensity has been possible due to nano-photonic advancements.[38] In the case of lasers, to overcome the limitations of a macroscopic dimensions, waveguiding mechanisms to couple electromagnetic waves within nanoscale dimensions have been explored.[3,39–41] Much of the progress in this regard can be attributed to the progress of Plasmonics. As such it is a hot topic of research in recent times.

Plasmonics are associated with the quanta of plasma oscillation known as plasmons. Plasmons can be broadly divided into two types based on their localization tendencies. Propagating plasmons (SPP) and localized surface plasmons (LSP). Other than that, some specialized plasmon modes can be exhibited in special metal-dielectric interfaces, such as Tamm plasmon polariton (TPP).

## 1.2.1   SPP: Surface Plasmon Polaritons

Surface plasmon polariton is an electromagnetic excitation propagating in a wave-like fashion along the planar interface between a metal and dielectric. These electromagnetic waves get trapped on the metal surface due to collective oscillation of the surface electron of metal. Lightwave causes free electrons on metal surface (Surface Plasmons, SPs) to oscillate collectively and resonate with the incident electromagnetic wave, generating SPPs. This two dimensional excitation decays exponentially with distance from the surface. Decay length in metal is on order of 10 nm which is comparable to skin depth and is two order of magnitude smaller than wavelength of light in air.[23] Because of confinement on metal surface, it shows a field enhancement which is extremely sensitive to surface conditions. Proper tailoring of metal surfaces can help control properties of surface plasmon and give opportunities to explore subwavelength optics.[42]

Interest in this field has increased as the fabrication technology for nanoscale manipulation of metal has advanced. This has made it possible to tailor SPs for specific applications. Use of SP has been already explored in a lot of sectors, such as in solar cells, biosensors for detection of biomolecules, lasers, raman spectroscopy, data storage etc. The first appearance of SP came in literature in 1950.[43] Physical significance of SPP lies in photons coupling to collective excitation of conduction electron on metal surface. The physics behind SPP lies mainly in the difference of permittivity between metal and the surrounding material. Due to this difference light gets concentrated in sub-wavelength dimensions and an amplified electric field can be seen. Electric field perpendicular to the surface decays exponentially with distance from the surface resulting in an evanescent nature which prevents power propagating away from the surface. SPP cannot radiate light in dielectric medium and cant be excited using conventional light from adjacent dielectric.[44] For a given energy, the photon wave vector $k$ is less than the SP wave vector $k_{sp}$ as can be seen from Fig. 1.2. As the SPP mode has higher momentum it can't be coupled directly on plane metal by incident light. To generate SPs on metal interface incoming photons must be coupled using a grating, prism or period corrugations on metal.[2,42] SPP mode cannot be excited by perpendicular incidence of light on metal interface.
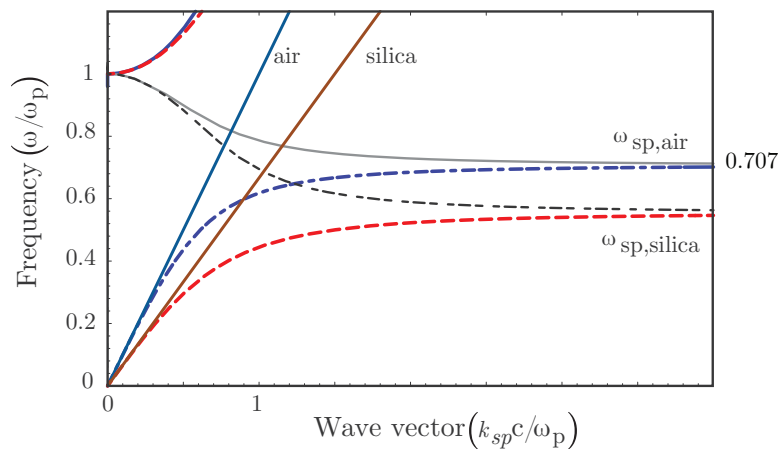


Figure 1.2: Dispersion relation of the SPP at the interface between a metal and air (blue) and silica (red).[2]

Electromagnetic field at the surface is obtained by solving Maxwell's equation with appropriate

boundary conditions. Only transverse magnetic (TM) or p-polarized light can couple to SPP; it is not possible to couple it using Transverse Electric or s-polarized light. The surface plasmon wave vector, $k_{sp}$ can be characterised by the dispersion relation:

$$k_{sp} = \frac{\omega}{c}\sqrt{\frac{\varepsilon_m \varepsilon_d}{\varepsilon_m + \varepsilon_d}} \tag{1.1}$$

Where, $\varepsilon_m$ is the permittivity of the metal and $\varepsilon_d$ is the permittivity of the dielectric adjacent to the metal surface. $\omega$ and $c$ indicate the frequency and speed of light. From the equation, the SPP dispersion curve must lie right to the dispersion curve of light in dielectric medium $k = \omega/c$ or dielectric light line so that the condition of SPP decaying exponentially with distance from surface is true. For coupling of SP, according to the above formula metal and dielectric are great choice as metal has negative and complex permittivity.

SPP based circuits can help in overcoming diffraction limit and merging photonic and electronic circuit solving the compatibility issue. Optical waves of 1000 nm length are generally used in photonic circuits.[23] When the optical device dimension is near wavelength, diffraction hinders the propagation of light. Surface plasmon technology provides the opportunity to confine light energy in very small dimensions. By the use of surface plasmons, diffraction limit can be overcome and device dimensions can be further miniaturized.

## 1.2.2   LSP: Localized Surface Plasmons

This surface excitation exists on bounded geometries like metallic nano-particles (MNPs) or voids. Unlike SPPs, LSPs are not able to propagate freely, but are confined to metallic nano-structures. As such they can show very high near-field enhancement. Also, the LSP resonance can increase absorption in the surrounding medium. Its dispersion relation depends on discrete, complex frequencies which depend on size and shape of the metallic nano-particles and its dielectric function. As LSP is confined to a small volume, it results in high field enhancement. Also, increased absorption can be seen at the LSP resonant frequencies. The plasma resonant frequency in an LSP depends upon the particle shape and surrounding environment.[45,46] The optical absorption leads to the metal nanoparticles appearing in different colours because of their shapes. The spectrum of LSP for an array of particles or holes depend on the interaction between individual LSP resonances. And the LSP resonance for individual metallic nanoparticles (MNPs) is different from the resonance of the array of MNPs. The coupling of individual LSP resonances can be thought of as interacting dipoles[2] whose strength of interaction is increases with closer packing of the array MNPs. The near field interaction between LSPs in arrays, causes shift in plasmon resonance and changes the spatial field distribution. The scattering of EM waves from arrays of MNPs is drastically reduced for closely packed array of MNPs.[47–49]

Major problem of SPP is the loss due to absorption in metal. Due to ohmic losses (which occurs due to metal having imaginary part of dielectric constant greater than zero) resistive heating occurs. Energy carried by SPP decays along propagation surface. Ohmic loss can be addressed by reducing metal volume. An array of nanoparticle cavities or nano-hole array (NHA) can be used as a waveguide for reduced metal

volume. As such, LSPs are slightly less affected by ohmic losses. There is trade off between mode size and propagation loss. Higher mode size results in smaller propagation loss and vice versa.[23] However, the MNPs associated with LSP resonance, can be surrounded by gain media, to overcome the losses and amplify the LSP response. The complex and negative imaginary permittivity in gain media, can strengthen plasmon resonance.[50]

Various plasmonic nanostructure can couple both long and short range SPP mode. Long range SPP mode dissipate less energy thus have a long propagation length on the order of millimeter in telecommunication frequencies .But this mode does not show subwavelength localization. Short range SPP mode on the other hand have higher dissipation energy, shorter propagation length but is able to show subwavelength localization making it a better choice for integrated optics. Mode localization increases with decrease in lateral dimension of waveguide for short range SPP, with increasing dissipation.Such loss can be dealt with by adding an active gain media in dielectric adjacent to metal. Moreover at higher wavelength losses are significantly small, so SPP based lasers are designed in mid-infrared range to combat the drawbacks.[22]

## 1.3    State-of-the-art and Overview of Thesis

Research on multi-mode and dual-mode plasmonic lasers have attracted attention only recently. The first multi-modal plasmonic laser has been reported in 2017, which exploited multiple band-edge modes that are excited by resonance from plasmonic superlattices consisting of periodic nanoparticles on periodic patches.[51] By grouping nanoparticles into a patch and repeating it periodically to form an array of such patches, Wang et al. obtained dual-mode lasing.[51] However, such devices become large as a single unit cell, or the patch periodicity is 24 $\mu$m. Wang et al. obtained an emission linewidth of <0.5 nm, a mode separation of ~10 nm and a divergence angle of <1° from their device, which had a centimeter-squared area.

More recently, ferromagnetic Ni plasmonic nanodisk array has been utilized for producing multimodal lasing, the device structure being within nanoscale dimensions.[52] Pourjamal et al. achieved dual-mode lasing by breaking the symmetry of the nanoparticle array using two different periodicities along the *x*- and *y*-directions of the 2D array. However, different periodicities along two axis generate additional spatial destructive interference, increasing the divergence angle, making it less coherent in the spatial domain than existing laser designs. They demonstrated dual-mode lasing in visible wavelength with a linewidth <1 nm, a divergence angle of ~5.7°, and of mode separation of ~15 nm. In Refs.,[51,52] the plasmonic nanoparticle array of the structure consisted of two-fold periodicity. More recently, a Quantum-Dot Plasmonic Lattice Laser has also shown to exhibit dual-mode emission.[53]

The goal of our thesis was to design an efficient and well separated dual-mode laser that would have more than one lasing mode emission simultaneously. The importance of such work can be easily understood in the current as well as the near-future scenario from the discussion in section 1.1.1. Dual-mode plasmonic lasers on the have ample scope contribution in the field of Optical Interconnects,[16–21] sensing and measurement.[10–13] Keeping the goal in our mind we explored many structures and played around with various topology to get our desired result. We have presented here our workflow, methodology, and corresponding results of our design respectively. In chapter 1 we gave a brief discussion about

plasmonics and dual-mode lasing, focusing on the state-of-the-art and the usefulness of research in this field. In chapter 2 our simulation methodology and material modeling have been presented. We simulated our device using the FDTD algorithm to solve Maxwell's Electromagnetic equation with the help of Lumerical FDTD software. Following that, in the same chapter we presented our material model for materials used throughout the proposed device, and presented four levels two-electron model for the analysis of laser gain media. We verified our methodology by reproducing a reputed published work. In the next chapter,i.e chapter 3 we introduced an analysis of the gain media used in our structure. We looked deeply into how gain material behavior depends on a various design parameters such as doping concentration and pump intensity, and how to design the gain for optimum performance. In chapter 4, we discussed the workflow for designing the cavity that would support dual-mode lasing. We took various approaches to find out optimum cavity design. In our structure, we incorporated Extraordinary transmission through metal NHA and Optical Tamm state at the surface to get improved performance compared to conventional plasmonic structures. We have talked about two different approaches to generate a dual resonant structure. First, by introducing dual periodicity in the NHA and later by adding a complex dual photonic crystal (PhC). In the first approach, we added two different periodicities of nano-hole array so that each can help generate a resonance mode. In the second approach, connecting multiple photonic crystals creates the ability to support multiple modes. We looked deeply into different parameters, hole width, depth, periodicity, metal layer thickness, photonic crystal layer thickness, number of layers, and other different parameters to design the cavity which will be used later as the gain medium of the laser by doping with dye molecule. The following chapter focuses on laser performance. We presented our work on how well the designed laser works for various conditions, threshold, the directionality of lasing emission, and tuning mechanisms. In the last chapter, we presented the concluding remarks for our journey with the thesis and suggested some scope of future works for enhancing and playing with our design to improve and mend our designed laser performance to suit application-based needs.

# Chapter 2

# Simulation Methodology and Modelling

To simulate the laser structures and observe the lasing performance we executed time domain and frequency domain analysis. To this end, we chose to use a method based upon the finite difference time domain (FDTD) algorithm for computing the electromagnetics involved in the whole process. The FDTD solutions module of Lumerical Inc. is one such software, which is based upon the FDTD algorithm.[54] This software has been used in all of the electromagnetic simulations and calculations.

## 2.1 FDTD Methodology for Electromagnetic Simulations

FDTD algorithm in computaional electrodynamics is a well established technique that solves Maxwell's electromagnetic equations. This technique overcomes the difficulties associated with frequency domain techniques as it solves the associated differential equations in the time domain on a spatial grid, using central difference approximations. This has enabled the FDTD technique to provide responses from a large range of frequencies in just a single simulation run. It is robust and supports large number of system parameters. In solving the system of equations through quantizing space, greater random access memory (RAM) support is required. This has proved to support better visualization. Thus, coupled with the advances in computational prowess, this technique has garnered much popularity since the 1980s.

### 2.1.1 FDTD Algorithm explained

FDTD technique is a space-grid time domain technique that numerically solves Maxwell's curl equations (Eq. 2.1) using finite central difference method. Firstly, Maxwell's curl equations are discretized in time

and space domain, using the finite difference method.

$$\frac{\partial \vec{E}}{\partial t} = \frac{1}{\varepsilon_0 \varepsilon_r} \nabla \times \vec{H} \tag{2.1a}$$

$$\vec{D}(\omega) = \varepsilon_0 \varepsilon_r(\omega) \vec{E}(\omega) \tag{2.1b}$$

$$\frac{\partial \vec{H}}{\partial t} = -\frac{1}{\mu} \nabla \times \vec{E} \tag{2.1c}$$

$$\vec{B}(\omega) = \mu_0(\omega) \vec{H}(\omega) \tag{2.1d}$$

The space grid lattice is known as mesh. Each of the unit cell in this cartesian grid lattice is known as a Yee grid. Each of the $\vec{E}$ component in space is surrounded by four other $\vec{H}$ components which are circulating. Thus, any $\vec{E}_z$ component in the yee grid is surrounded by $\vec{H}_x$ and $\vec{H}_y$ components. If we consider propagation along z axis, then these the components together form, what is known as Transverse Magnetic (**TM$_z$**) mode. Similarly, for the same propagation axis, an $\vec{H}_z$ component surrounded by circulating $\vec{E}_x$ and $\vec{E}_y$ components is a Transverse Electric (**TE$_z$**) mode. This is how, Maxwell's equations
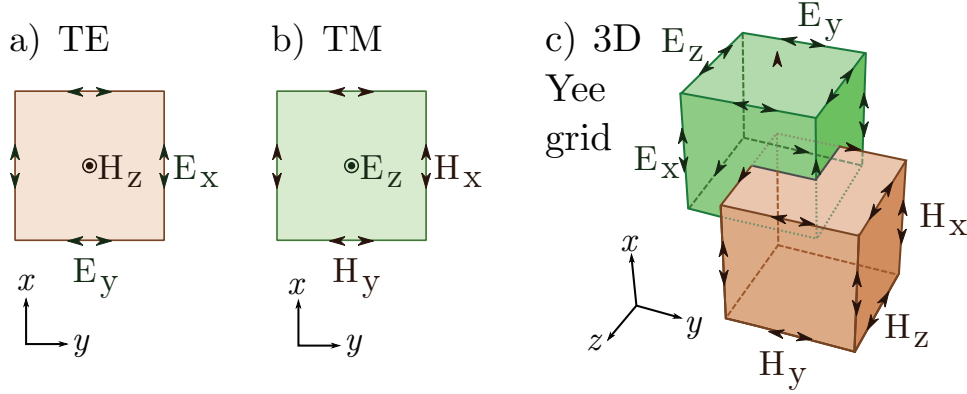


Figure 2.1: The Yee grid unit cell. The Maxwell's equation can be split into TE and TM modes. (a) The 2D *xy* planar grid showing Transverse Electric mode. (b) The 2D *xy* planar grid showing Transverse Magnetic mode. (c) A unit cell in Yee grid showing the staggered formation of $\vec{E}$ and $\vec{H}$ components in space.

can be split into two independent set of equations which solve for three vector quantities in each. These two mode components together can give a view of the total electromagnetic radiation over a greater expanse of the Yee grid. It is also important to note, that in time domain, the $\vec{H}$ (i.e $\vec{H}_x$, $\vec{H}_y$ and $\vec{H}_z$) and $\vec{E}$ (i.e $\vec{E}_x$, $\vec{E}_y$ and $\vec{E}_z$) fields are staggered in time and space, i.e both fields are not attainable at the same point or time instant. Then the system of discrete differential equations are solved simultaneously, at each point in each time step in a leapfrog manner.

$$\vec{E}(t + \Delta t) = \vec{E}(t) + \frac{\Delta t}{\varepsilon} \nabla \times \vec{H}(t + \Delta t/2) \tag{2.2a}$$

$$\vec{H}(t + \Delta t/2) = \vec{H}(t - \Delta t/2) + \frac{\Delta t}{\mu} \nabla \times \vec{E}(t) \tag{2.2b}$$

The equations 2.2 dictate the method of updating $\vec{H}$ and $\vec{E}$ component values for next time step, from the data available at given time step. It is to be noted, that $\vec{E}$ and $\vec{H}$ values are calculated at $n\Delta t$ and $(2n+1)\Delta t/2$ time instants respectively, where $n$ is a positive integer. This method of staggered time

domain evaluation is known as leapfrog method. For the equations below, $\varepsilon = \varepsilon_0.\varepsilon_r$, is the permittivity and $\mu = \mu_0.\mu_r$ is the permeability of the medium in consideration. It is evident that from Ampere's circuital law, the $\vec{E}$ field that is obtained at a particular time step is related to $\vec{H}$ field and $\vec{E}$ field data at previous time steps. This $\vec{E}$ component data is incorporated into the modified Faraday's law, along with $\vec{H}$ data from previous time step to obtain $\vec{H}$ data at given time step.

The FDTD algorithm, solves the coupled Maxwell's equation, as opposed to just solving for only $\vec{E}$ field (or $\vec{H}$ field). This makes the technique much more robust than frequency domain methods.

## 2.1.2 Cell Size and Time step

In order to compute the space derivatives of the associated fields, resolution of the Yee solver grid must be specified. As wavelength of EM radiation is a material dependent parameter, the refractive index of a material will affect the wavelength of radiation. As a rule of thumb, a resolution, $\Delta x$ that is at least 10 times smaller than the minimum wavelength $(\Delta x \leqslant \frac{\lambda_0}{n_{max}.10})$ in the simulation region should give proper results. The space lattice may either be uniformly structured throughout the simulation region or it may support non uniform Having determined the spatial grid resolution, we can go on to determine the minimum time resolution of the simulation. From the Courant condition we can conclude that minimum time step is $(\Delta t \leqslant \frac{\Delta x}{\sqrt{d}.c_0})$

The time and space resolution are important parameters in any FDTD simulation. The spatial resolution determines the accuracy of the obtained solution, while the appropriate time resolution is necessary to ensure stability and convergence of simulation results.

## 2.1.3 Boundary Conditions

### Perfectly Matched Layers - PML BCs

The absorbing boundary condition (ABC) in FDTD simulation is essential in cases, where, the simulation region extends upto infinity. Such a boundary ensures that all of the incident radiation is absorbed at the boundary while also maintaining continuity throughout the interface. In Lumerical Inc. the perfectly matched layer (PML) boundary condition is used as an absorbing boundary. This ensures that reflection and scattering from the boundary does not take place within the simulation region. A PML boundary condition at the simulation edges will add extra lossy layers at the simualation boundary. More the number of layers, more the absorption and hence better the accuracy of the solutions. However, the simulation time is also increased because of it.

### Periodic BCs

Periodic boundary conditions are utilized for simulating periodic systems. If the structure and the wave source has symmetry in its unit cell, then appropriately symmetric and anti-symmetric boundary condition can be applied on the boundaries where the periodic condition was used. This has the ability to reduce simulation region by 2 (symmetric along one axis), 4 (symmetric along two axis) or 8 times (symmetric

along all three axis). Thus correctly applying this boundary condition can help save much computation time.

**Bloch BCs**

Bloch boundary condition is a special case of boundary condition that is used for angled plane wave source. An angled plane wave source doesn't solve correctly under periodic conditions as, the plane wave has a phase difference at the periodic boundary. This problem can be eradicated by using Bloch boundary conditions for angled planewave source.

In this work, we have simulated and tested a model gain medium for the production of laser using the FDTD solver. In the whole modelling process we have tweaked some of the intrinsic parameters of the gain medium used in this model; such as the doping concentration of dye molecules, the amplitude of the input optical pump and the lifetime of the electron transitions during the lasing operation. To accurately and effectively validate the model of our gain medium, we have used a finite difference time domain (FDTD) simulator to solve the time dependent Maxwell's third and fourth equations. As this is a time domain method, the process is robust and offers a good overview of the associated electromagnetic and photonic aspects of the system.[55]

In solving the differential equations, we selected the boundary conditions appropriately and specified the desired material model of the gain medium. It was of significant importance to select the proper boundary conditions because of the computational limitations and leakage associated with the simulator. The parameters of the material model of the gain medium was also continuously readjusted while testing. The FDTD method is a grid based modeling method, where the time dependent Maxwell's equations are quantized using central difference approximations in both spatial and temporal derivatives. Then, the finite difference equations which are formed. The electrical field vector is solved in the grid at a given instant. Then the magnetic field vector are in the same spatial volume is solved next by the formed equations. This process is iterated to obtain the required transient or equilibrium electromagnetic field.This algorithm of solving Maxwell's equations in this paper, is based upon a method proposed by Yee.[56]

## 2.2   Gain Medium Modelling: The Four-Level Two-Electron Model

In this section we enunciate the gain medium modeling mechanism. Thereafter, we simulate the lasing dynamics of the gain medium using the devised model. The gain medium of the devised laser structure in this work, uses a gain medium composed of dye molecules embedded in a polymer host matrix. The gain medium which is used in the simulation, utilizes a four level two electron atomic system. In this simplified model, the dye molecules embedded in the laser material acts as the gain medium and provides the four discrete electron energies for each of the two interacting electrons.[57,58] The model abides by Pauli's Exclusion Principle and the electron dynamics is governed by the coupled rate equations of the four level system.[1] A simple photonic cavity laser is simulated and the results are verified. After verification, the next section is devoted to the parameter analysis of this gain medium, using this model.

The four level system along with the associated parameters is shown in figure 2.2. This system is treated
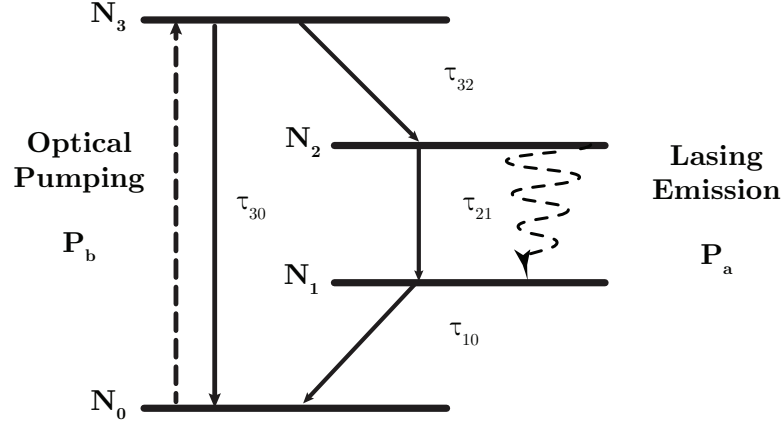


Figure 2.2: The four level two electron model

quantum mechanically while the optical pump input is treated classically. Electronic transition takes place from level 0 to level 3 due to induced absorption from the electromagnetic pump. Almost instantly, there is a spontaneous non-radiative emission due to transition of that electron to level 2. The radiative and stimulated emission takes place due to transition from level 2 to level 1 by time $\tau_{21}$. The stimulation for such a downward transition needs to be caused by a stimulant. In absence of a stimulant spontaneous emission occurs. Stimulant of energy equal to the energy difference between level 2 and 1 can be applied by a cavity feedback. Or the stimulant may be an externally provided probe pulse of same energy. Finally another induced emission forces the electron to level 0 in short time. Transitions from level 0 to level 3 and level 2 to level 1 can be considered as two dipole oscillations; corresponding to polarization densities $P_b$ and $P_a$ respectively. They are found to be guided by the equations:

$$\frac{\partial^2 P_a}{\partial t^2} + \gamma_a \frac{\partial P_a}{\partial t} + \omega_a^2 P_a = \zeta_a (N_2 - N_1)E \tag{2.3a}$$

$$\frac{\partial^2 P_b}{\partial t^2} + \gamma_a \frac{\partial P_b}{\partial t} + \omega_b^2 P_b = \zeta_b (N_3 - N_0)E \tag{2.3b}$$

Here, the constant $\zeta_{a,b} = 6\pi\varepsilon_0 c^3/(\omega_{a,b}^2 . \tau_{21,30})$ and damping coefficients are $\gamma_{a,b}$. Here, $\omega_b$ is the resonant frequency associated to the energy gap between level 0 and 3. While $\omega_a$ is the resonant frequency associated to the energy gap between level 2 and 1. Due to the constraints of Pauli's Exclusion Principle (PEP), the presence of electrons in one energy level limits the rate of electron transitioning (hence pumping) from other energy levels. So the rate of electron transitions from an energy level is dependent on the population of the associated levels. Thus the rate equations become:

$$\frac{dN_3}{dt} = -\frac{N_3(1-N_2)}{\tau_{32}} - \frac{N_3(1-N_0)}{\tau_{30}} + \frac{1}{\hbar\omega_b}E.\frac{dP_b}{dt} \tag{2.4a}$$

$$\frac{dN_2}{dt} = \frac{N_3(1-N_2)}{\tau_{32}} - \frac{N_2(1-N_1)}{\tau_{21}} + \frac{1}{\hbar\omega_a}E.\frac{dP_a}{dt} \tag{2.4b}$$

$$\frac{dN_1}{dt} = \frac{N_2(1-N_1)}{\tau_{21}} - \frac{N_1(1-N_0)}{\tau_{10}} + \frac{1}{\hbar\omega_a}E.\frac{dP_a}{dt} \tag{2.4c}$$

$$\frac{dN_0}{dt} = \frac{N_3(1-N_0)}{\tau_{30}} + \frac{N_1(1-N_0)}{\tau_{10}} + \frac{1}{\hbar\omega_b}E.\frac{dP_b}{dt} \tag{2.4d}$$

$$\tag{2.4e}$$

13
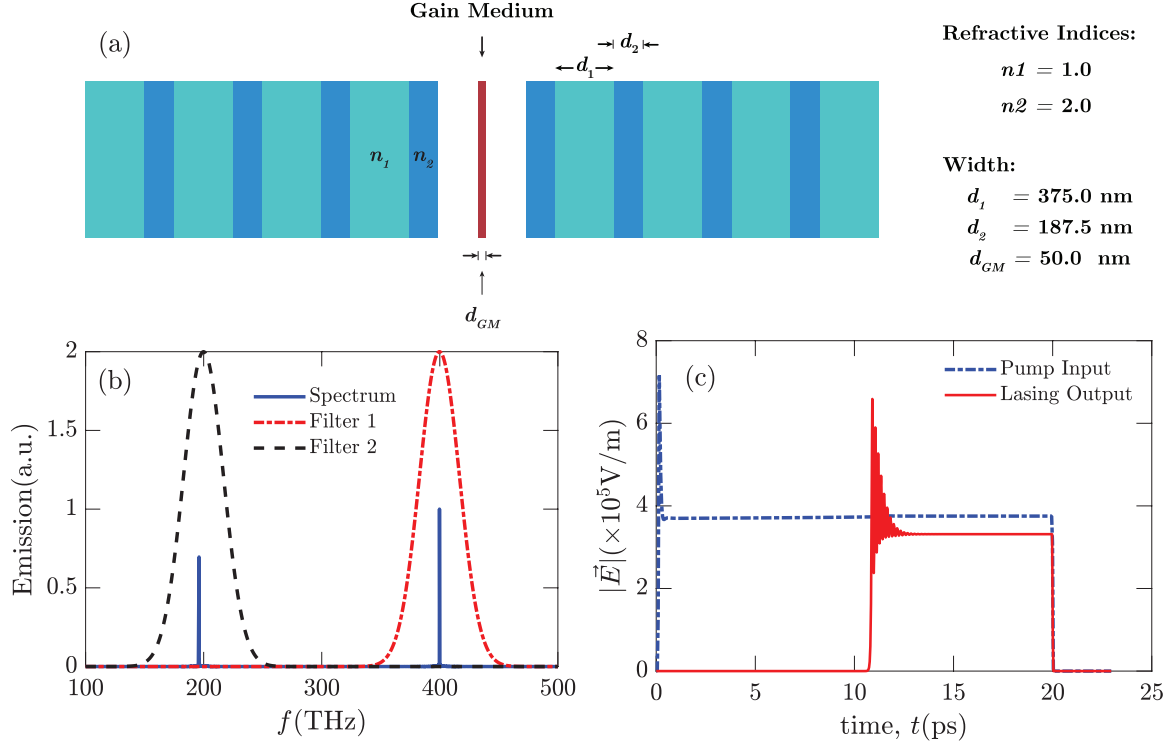
Figure 2.3: (a) Schematic of the simple photonic cavity laser with two DBRs along with necessary parameters. (b) Obtained EM spectrum with Gaussian filters to extrapolate pumping and lasing emission separately. (c) Time response of pump signal and lasing signal obtained from the output side of the PCL

Here, $N_i$ is the population density probability in level $i$ and $\tau_{ij}$ is the relaxation time from level $i$ to $j$ and vice versa. This model is relates equation 2.3 with Maxwell-Ampere law by the following equation:

$$\frac{\mathrm{d}E}{\mathrm{d}t} = \frac{1}{\varepsilon}\nabla \times H - \frac{1}{\varepsilon}N_D\left(\frac{\mathrm{d}P_a}{\mathrm{d}t} + \frac{\mathrm{d}P_b}{\mathrm{d}t}\right) \tag{4}$$

Here, $N_D$ is the electron population concentration in the model. If each dye molecule in the host matrix provides one electron, $N_D$ is also, the the concentration of the dye molecules which are embedded into the host matrix of the laser gain medium.

## 2.2.1   Model Verification: Simple Photonic Cavity Laser

To verify this material model, we simulated a simple photonic laser using this gain medium. The effect of the gain medium in a one dimensional, optically pumped, single defect, Distributed Bragg Reflector (DBR) laser cavity was observed. Fig. 2.3(a) shows the schematic of the structure with parameters. The DBR cavity consisted of a 750 nm gap between the two DBRs. This corresponds to a cold cavity defect mode of 1500 nm. Each of the Bragg Reflectors had four layers of alternating refracting indices, alternating between 1 and 2 with thickness $\lambda_a/4 = 375$ nm and $\lambda_a/(2 \times 4) = 187.5$ nm respectively. In the middle of the gap we placed our gain medium of 50 nm thickness. The structure was pumped with a light of 750 nm as the energy difference between the optical pumping levels corresponds to this wavelength of photon.

The optical pump input was a continuous EM plane wave of 750 nm wavelength, which increases monotonically to its steady state amplitude of $1 \times 10^6$ V/m within a short time. This modification was

introduced to reduce the noise infiltration. The DBR passband and stopband are centered at 750 nm and 1500 nm respectively. Lasing emission occurs at 1500 nm, corresponding to the energy difference between the lasing levels. within the cavity. The values of the parameters for this structure tabulated in table 2.1 have been obtained from Ref.[1]

For sustained lasing, the value of $\tau_{30} = \tau_{21}$ must be larger than $\tau_{32} = \tau_{10}$, which was true for this case.

| Parameter | Value |
|---|---|
| Absorption wavelength ($\lambda_b$) | 750 nm |
| Emission wavelength ($\lambda_a$) | 1500 nm |
| Index of gain medium base material | 1.21 |
| Dye Concentration | $6 \times 10^{17}$ cm$^{-3}$ |
| Transition Lifetimes: | |
| $\tau_{30} = \tau_{21}$ | 300 ps |
| $\tau_{32} = \tau_{10}$ | 100 fs |

Table 2.1: Value of the parameters of the 4-level 2-electron gain medium model used in simulation.[1]

As the structure is symmetric lasing action occurs in both directions. The obtained emission intensity spectrum exhibited two clear modes at pumping frequency 400 THz corresponding to 1500 nm and at the lasing frequency, 200 THz corresponding to 750 nm. The two peaks are subjected to Gaussian filtering in the frequency domain. Separate Gaussian filters centered at pumping frequency of 400 THz and lasing frequency of 200 THz was used to extract the two signal components at different frequencies. This separated the lasing and pumping modes. By using inverse fourier transform the time domain lasing signal at 200 THz and pumping signal at 400 THz was obtained separately.

The lasing emission is seen to be slightly lesser in intensity than the pumping signal. The time response of the individual pumping and lasing modes as seen from Fig. 2.3(c) have a time delay of about 11 ps between them. This delay is concurrent with the inception of population inversion between level 2 and
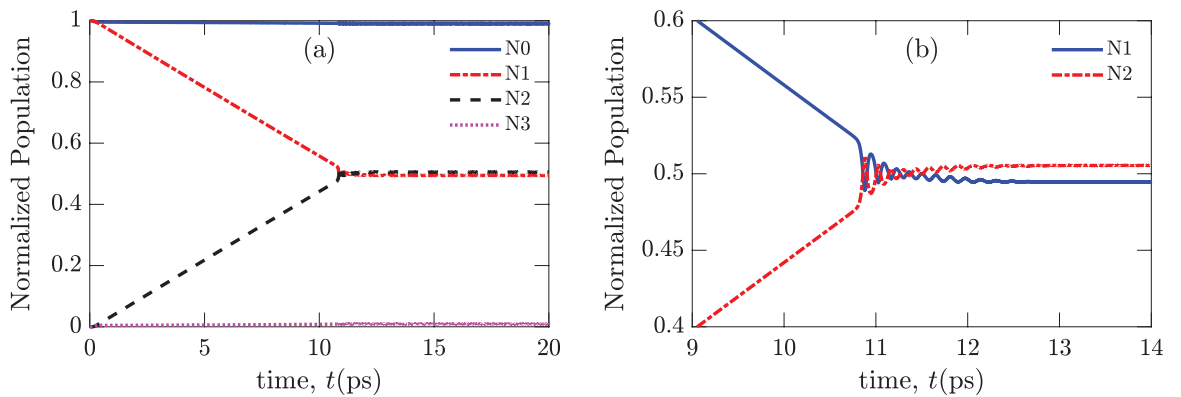


Figure 2.4: (a) Variation of normalized electron population level with time. (b) Zoomed in population of level 1 and 2 showing sustained population inversion from 11 ps.
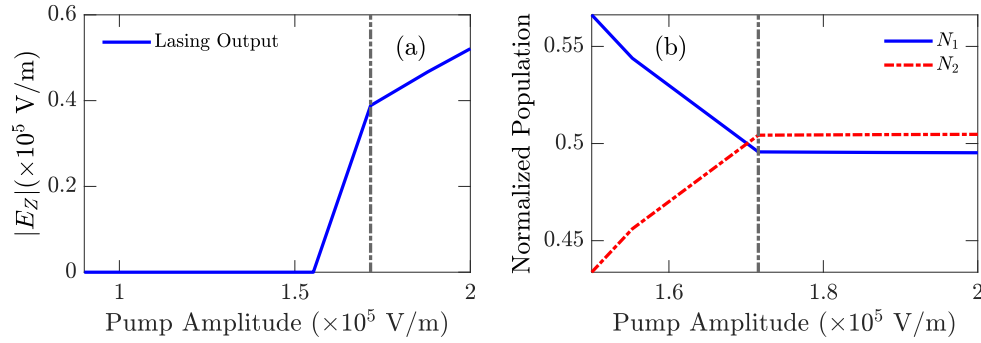
Figure 2.5: (a) Variation of normalized electron population level with time. (b) Zoomed in population of level 1 and 2 showing sustained population inversion from 11 ps.

1. The time variation of the normalized electron population density variation at different levels is seen in Fig. 2.4. The initial electron population before pumping was contained in level 0 and 1. Hence, at $t = 0$, $N_0 = N_1 = 1$. With time, level 3 gets populated, which is rapidly transited to level 2. So, electrons are pumped from level 0 to level 2 via level 3. Fig. 2.4 shows that right after 11 ps, there is sustained population inversion between level 2 and 1. The transient behaviour of the lasing signal can be attributed to the transient behaviour of the population levels during the initial time frame of lasing action. The results simulated are well in agreement with the discussion and results mentioned in Ref.[1]

The defining characteristic of a laser gain medium, is its threshold behaviour. A precise definition of threshold can be given as, the condition for which, spontaneous and stimulated emission rates are equal.[30] At energies below which, spontaneous emission dominates, lasing does not occur. Below threshold, the non-radiative emissions dominate. However, as the device dimensions have reduced over the years, the typical threshold behaviour concept of macroscopic lasers have become obsolete. For nanocavity lasers, the threshold is greatly reduced.[59,60] The loss due to the transmission through the Linear asymmetric DBR pair photonic cavity causes the threshold. So, lasing emission is observed when, the input pump of the lasing system, crosses a minimum value, i.e the threshold. The output lasing intensity versus the input pumping intensity was plotted as shown in Fig. 2.5. There is a clear threshold at $1.7 \times 10^5$ V/m, which is indicative of the minimum energy barrier that is needed to initiate lasing.

# Chapter 3

# Gain Medium Analysis

The essential component of any laser system is a gain medium. It functions as the light amplification component and the material model of the medium enables the observation of amplification. At the core of the proposed plasmonic lasers' optical cavity, the gain medium consists of IR-140 dye molecules embedded in polyurethane (PU) matrix. The parameters of this gain medium is tabulated in Table 3.1. The dye molecules offer gain to the incident pump energy. The IR-140 dye works in the near-IR regime, which has a host of application scopes ranging from spectroscopy,[61] to communication links in photonic/optical ICs.[62]

In the previous chapter we looked at the mathematical model used to define a Four-Level Two-Electron Model gain material model, used in some basic laser systems. From the coupled rate equations, we obtained the temporal population model of the system. thereafter a simple photonic laser system was

| Parameter | Value |
|---|---|
| Absorption wavelength ($\lambda_b$) | 800 nm |
| Emission wavelength ($\lambda_a$) | 870 nm |
| Index of gain medium base material | 1.51 |
| Dye Concentration | $2 \times 10^{18}$ cm$^{-3}$ |
| Transition Lifetimes: | |
| $\tau_{30} = \tau_{21}$ | 1 ns |
| $\tau_{32} = \tau_{10}$ | 10 fs |

Table 3.1: Parameter values of the 4-level 2-electron gain medium model of the IR-140 dye used in simulation.
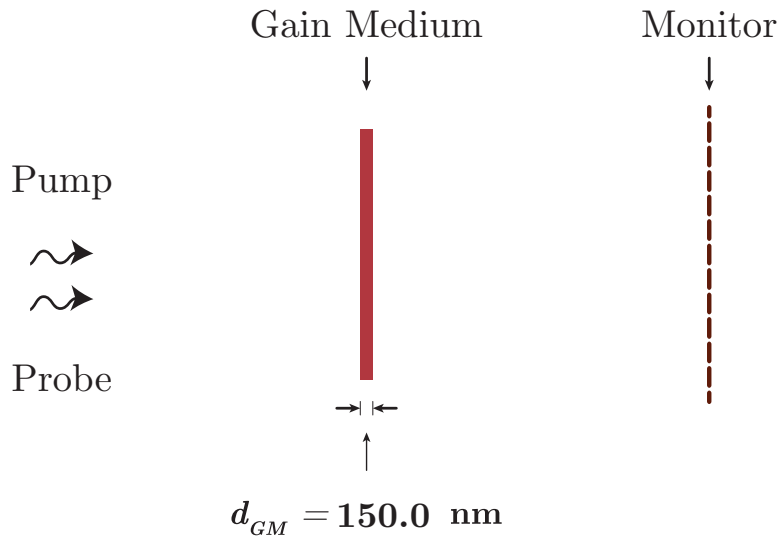
Figure 3.1: Simulation setup for the pump probe analysis.

implemented using a customized laser material, having taken the parameters from.[1] In this chapter we study the gain dynamics of IR-140 dye in a Polyurethane host medium, that gives lasing in the near IR regime. The essential parameters of the IR-140 have been taken from the works previously reported by.[58,63] To analyze the material model, a pump-probe spectroscopic analysis has been simulated to get the transmission spectrum of the given gain medium. In our detailed analysis we presented the spectral properties of the gain medium under different conditions. The following parameters were tuned to study the lasing performance of the gain medium. The variation of the peak transmission emission

- **Dye molecule concentration**

- **Input Pump energy**

## 3.1   Pump-Probe analysis

Pump-probe is used in spectroscopic analysis to determine the absorption and transmission of substances in response to electromagnetic excitation.[64] In lasers, a pumping signal excites the ground state electrons to higher state. Compared to the pump pulse strength, the meager probe pulse seeks to just stimulate the already excited atoms to emit energy, thus causing stimulated emission. For better resolution of the gain medium characteristics, pump-probe analysis is an effective tool to study spectral characteristics, as it offers real state spectra and time resolution of sufficient quality. The absorption of pump and amplified transmission of lasing emission can be studied by a pump-probe analysis of lasers. Hence, it is a good tool to characterise gain medium performance. In a gain medium, there is amplification of the lasing mode. Usually, a laser has greater than unity transmission at the lasing mode, often up to tens of orders of magnitude higher than unity. For the IR-140 dyes, the lasing mode is at 870 nm. In this analysis, the transmission spectrum of the gain medium shows an enhanced transmission, at 870 nm.

 The simulation setup for a pump-probe analysis is very simple. The pumping source and probing souce are kept at the same side of the 150 nm thick gain media at same location. They are 7 $\mu$m apart from the

18

gain medium centre. A frequency monitor is placed at the opposite end as shown in Fig. 3.1 to calculate the net transmission/absorption spectra. The monitor is kept 8 $\mu$m away from the centre of the gain medium. The pump generates an 800 nm wavelength plane wave pulse of 4 ps pulse length. Unless otherwise mentioned, the pumping electric field amplitude was $2 \times 10^6 \text{V/m}$. The probe signal was just an extremely short impulse of 870 nm wavelength applied after 30 ps; well after the pumping pulse has died out. The IR-140 doping concentration of PU host matrix was kept at $2 \times 10^{18}$ cm$^{-3}$ unless otherwise mentioned.

## Dye molecule concentration variation

By tuning the concentration of dye molecules in the gain medium, we observed changes in the lasing emission. There is an observable threshold value of concentration below which lasing does not take place. We can account this behaviour to the population inversion between level 2 and 1 that is needed for lasing action. The number of photons absorbed is proportional to the population level at the two lower levels 1 and 0, i.e the density of the dye molecules in the host matrix. The lasing emission is proportional to the population at level 2. So, at sufficiently low dye molecule concentrations, the number of electrons which are needed to be pumped up to level 2 is not available. Thus, the condition of population inversion $N_2 > N_1$ does not occur until a threshold value of dye concentration is reached. As we increase the dye molecule concentration, the lasing transmission is close to unity for . Beyond this optimum population level, the laser output changes almost arbitrarily, showing successive peaks and dips. The peak transmission starts to decay from about $8 \times 10^{21}$ cm$^{-3}$ increasing dye molecule concentration. This can be attributed to the effects at higher dye concentration. At higher dye molecule concentration, the inter-dye-molecular interactions degrade the effectiveness of the dye molecule, hence affecting the lasing output.[65] Mobility and concentration are important considerations that affect the photodeactivation of the dye molecules. these affect lasing output. Also, the operational lifetimes of the dye molecules is also shortened at higher concentrations. Thermal degradation of the dye molecule also becomes significant at higher densities. Each of the excited dye molecules can cause localized heat accumulation in the polymeric host material that is already has bad thermal conductivity. This enhances the photodegradation of the dye molecules.[66]
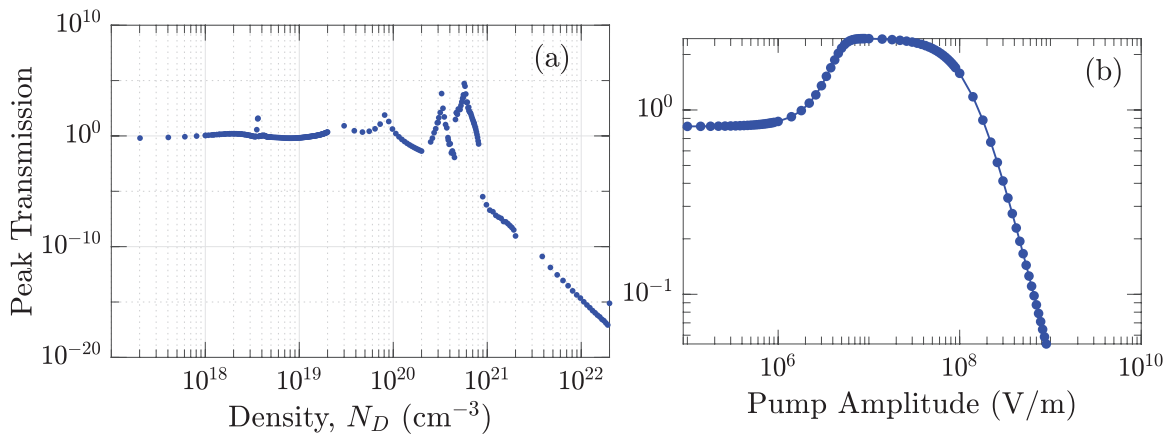


Figure 3.2: (a) The transmission at $\lambda_p = 870$ nm is plotted along $y-$axis and the doping concentration of the dye molecules in the gain medium is plotted along $x-$axis (b) Behaviour of the transmission, at same wavelength, for varying pump amplitude.

**Input Pumping intensity**

The laser model in the theoretical the treatise of Chang et. al.,[1] showed a threshold behaviour as seen in Fig. 2.5. There is a clear threshold at $1.7 \times 10^5$ V/m, which is indicative of the minimum energy barrier that is needed to initiate lasing. In the pump probe analysis, using IR-140 dye molecule parameters, The transmission at lasing wavelength, shows a threshold at $5 \times 10^6$ V/m. Transmission remains constant until there is a gradual drop, for pump amplitude greater than $1 \times 10^8$ V/m.

In this study of the solid state laser gain medium, involving IR-140 dye molecules, we simulated and modelled an appropriate simple cavity laser involving the given gain medium using an FDTD simulator. The dye molecules encapsulated in the polymeric host matrix formed the laser material. This medium was modelled by a 4 level 2 electron model. The intrinsic parameters were defined to produce lasing emission at a given wavelength. In addition to this, the lasing performance and efficiency at various dye concentration was observed. The threshold behaviour due to input pump amplitude variation was also observed and discussed. All the finding presented were consistent with the data obtained from the given references.

# Chapter 4

# Devising the Cavity Modes: EOT and OTS

A laser system, is comprised of mainly two components. The gain medium and the optical cavity. The optical cavity is also often known as 'optical resonator' as it amplifies the stimulated emission of lasers by of increasing the circulating power within the cavity. Traditional semiconductor laser systems which operate at 'micro' regime, have diffraction limited device dimensions and low modulation speeds. The miniaturization of photonic devices, has enabled nanoscale mode confinement and ultrafast lasing dynamics. And this has been possible due to novel nanocavity designs, which have enabled us to concentrate light to subwavelength regimes via plasmonic modes. Plasmonic nanocavity designs such as nanoparticle array[39,58,63] and gold nano-hole array (NHA) coupled with photonic crystal (PhC) structure[3] have been shown to produce lasing beyond the diffraction limit. Both these structures also exhibit considerable tuning capabilities. Recently, cavity designs which support dual-mode lasing have also been reported. These cavities utilized plasmonic nanoparticle superlattices,[51] Ni nanodisks[52] and quantum dots[15] respectively. However, as discussed in Chapter 1 the purpose of this work is to develop a dual-mode planar-multi-layer plasmonic laser, that can outperform the above mentioned dual-mode lasing counterparts. This chapter focuses on designing a plasmonic cavity which supports efficient dual-mode response without compromising device dimension and show good far field directionality.

## 4.1   A Tamm Plasmon assisted Planar laser Cavity

From the myriad of topology already available, we observe the cavity dynamics by observing the different phenomenon taking place inside the cavity that regulates the stimulated emission from the gain medium. A number of structures have already been reported to give desired dual resonant response.
A directional and efficient single mode planar plasmonic laser has been reported, which utilizes the application of modes excited at metal-PhC interface.[3] The single mode response is shown in Fig. 4.1. The design of a single mode plasmonic laser cavity is analyzed and dissected to observe the different tuning parameters available at our disposal. This laser shows a sharp spectral emission at $\sim 870$ nm. The
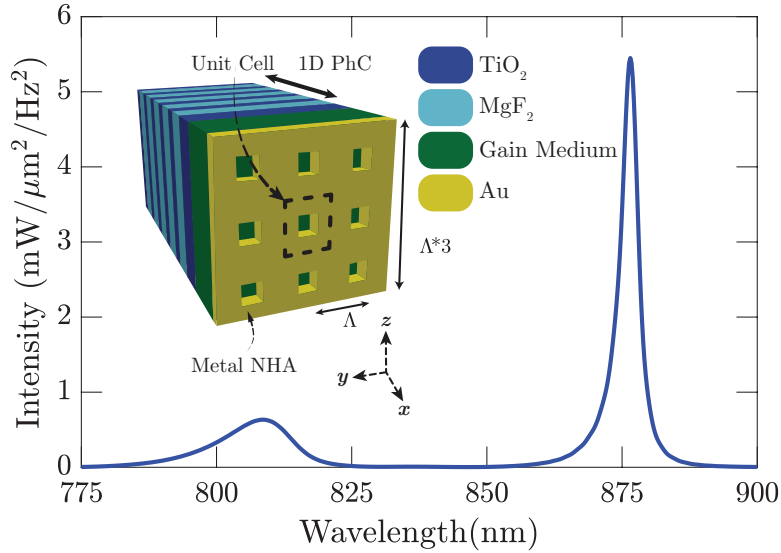
Figure 4.1: (a) Lasing emission from the schematic depicted in the inset. (Inset) Schematic of a single mode emitting planar multi-layer plasmonic laser.[3] The structure is pumped using a perpendicularly incident pump centered at 800 nm absorption wavelength. The number of alternating $TiO_2 - MgF_2$ layers in the DBR is 7. Here, the lasing peak is observed at $\sim 875$ nm.

resonator topology that has been exploited in this design ensures a single spectral mode at a specified wavelength, as shown in the response of the laser structure without incorporating the gain medium into the structure. This shows us that the cavity dynamics of the structure ensures a pronounced single peak at a certain wavelength. Different components of the entire structure plays its part in regulating the mode. On analyzing the structure, we find that the spectral position of the peak is affected by the final $TiO_2$ layer thickness and final gain layer thickness. This phenomenon has been attributed to the existence of Optical Tamm States (OTS) at the meta-crystal interface. They are also known as Tamm plasmon polariton (TPP), since plasmon-photon coupling occurs. Also, surface plasmon polariton (SPP) modes excite extraordinary transmission (EOT) on metal NHA interface in addition to Tamm Plasmon Polaritons (TPP). These two resonances couple together to create enhanced spectral cavity response. The spectral response strength and line-width at the lasing wavelength are strongly affected by the number of layers of the $MgF_2 - TiO_2$ pair.

However, none of the parameters of this particular design topology can be tweaked to produce more than one mode around the lasing wavelength. So, a new approach to design the cavity has been taken with the objective of generating the two (or more) lasing modes. Alongside, the physics has been explained with concepts already derived from existing literature. To exploit the nanoscale features of the existing design, we have explored two key avenues to tweak some of the features of this design altogether, exploring novel design techniques. We looked into tweaking the extraordinary transmission (EOT) phenomenon from the Au-NHA and the Optical Tamm States (OTS) associated with the DBRs. In the following sections we explore the physics of the entire design process where we end up with two prospective cavity designs. The physics of some of these phenomenon are explained, in order to better explain the phenomenon in terms of coupling of different plasmonic-photonic modes and tuning them.

## 4.2 Exploring concepts: Extraordinary Optical Transmission

Sub-wavelength hole array in metal film shows unique features in transmission spectrum, giving a series of peak and dip. This is known as extraordinary transmission. Due to EOT, transmission maxima normalized to hole area, can exceed unity. This feature can't be explained using standard aperture theory. Previously before the discovery of extraordinary optical transmission, sub-wavelength apertures were thought to be poor transmitter of optical energy. The transmission of light through single sub-wavelength aperture in an infinitely thin conducting screen, is associated with diffraction. If the aperture radius is much larger than the incident wavelength, the physics of the phenomenon can be explained quite successfully by Huygens-Fresnel principle. The normalized transmission coefficient for such structures is of the order of unity. However, Bethe[67] and Bouwkamp[68] were able to explain the transmission process for sub-wavelength apertures. The transmission coefficient was related to the aperture radius ($r$) and incident wavelength ($\lambda_0$) by equation 4.1

$$T \approx \frac{64}{27\pi^2}(\frac{r^4}{\lambda_0^4})$$ (4.1)

The transmission through sub-wavelength apertures can be amplified by arranging the holes into a periodic lattice structure. This phenomenon was named 'Extraordinary Optical Transmission' or EOT and was first reported by Ebbesen et al.[69] for a square array of cylindrical holes in a silver film. An enhanced transmission coefficient, normalized to the hole area, was observed for wavelengths greater than the array period. This is attributable to the enhancement offered by surface plasmon polariton (SPP) modes due to the periodicity of the nano-hole array (NHA). In producing EOT, the square lattice of NHA is active element. This becomes evident due to the exclusivity of the occurrence of EOT only for thin metallic films. The oscillation of surface charges must obey the following momentum matching condition, which relates the surface plasmon wavevector ($k_{sp}$) with incident photon momentum ($k_x = (2\pi/\lambda)sin\theta$) and the grating momentum wavevectors ($G_x = G_y = 2\pi/\Lambda$)

$$k_{sp} = k_x \pm iG_x \pm jG_y$$ (4.2)

From this relation, it has been observed that the transmission minima will coincide with the period of the NHA, $\Lambda$. The film thickness and hole dimensions have also been observed to influence EOT. These effects have been further analyzed in the transmission characteristics analysis presented later in this section. Also, from the dispersion relation of SP modes, we get

$$k_{sp} = \frac{\omega}{c}\sqrt{\frac{\varepsilon_m\varepsilon_d}{\varepsilon_m + \varepsilon_d}}$$ (4.3)

However, pure SP modes single-handedly cannot fully characterize EOT. Alongside SPP modes, EOT incorporates quasi cylindrical wave grazing along the surface. At sub-wavelength distances the SPP mode contribution to EOT spectrum is compromised.[70] There has also been strong correlation between hole shape and extraordinary transmission spectrum. Changing hole shape results in significant increase in EOT spectrum even though the lattice period, $\Lambda$ (hence the grating momentum wavevectors) remain constant. Square and rectangle shaped holes offered much greater transmission compared to circular holes in spite of having smaller surface area.[71,72] This effect has been attributed to 'shape' resonance in the NHA. An

in-depth detailed understanding of EOT resonance is necessary to be able to exploit this phenomenon in designing our desired dual-mode cavity. The physics behind EOT can be capitalized on and utilized to generate the desired dual-mode spectral output. To analyze the various effects and characteristics of EOT, we simulated a 100 nm thick Au film comprised of square array of nano-holes with the objective of finding a design for the Au-NHA, that gives a dual-mode response. Various NHA parameters were changed and the output response was evaluated.

## 4.2.1 Effect of Hole dimension
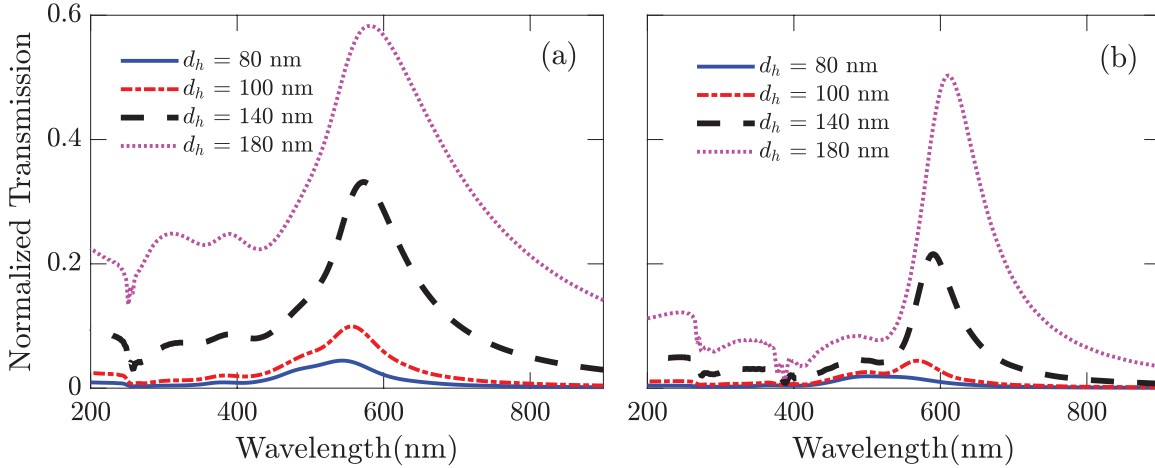


Figure 4.2: Normalized Transmission by varying hole width in Au metal thin film of 100 nm thickness perforated with square holes in square lattice, with period 250 nm (a) and 375 nm (b).Transmission peak gets redshifted when periodicity of NHA is increased as seen from (a) and (b). Also peak normalized transmission decreases with increase in periodicty.Spectral features remain almost identical despite increasing hole dimension. Transmission throughput is higher for a larger hole size. Maximum transmission peak shows a red shifting behavior and a broader peak width (FWHM) with increase in hole size.

To elucidate the effect of hole size in extraordinary transmission, we simulated an Au metal thin film of 100nm perforated with square hole in square lattice with period 250nm and another in period 375nm by varying hole width and the results are presented in Fig 4.2. Throughput of a metal hole array increases with hole size. Simulation shows that a larger hole size results in higher transmission maxima. Transmission peak gets shifted to longer wavelength for increase in hole width. The FWHM linewidth of peak gets broadened. A transmission minimum can be seen nearly fixed at 250 nm, which is the period of the square lattice. The increase in transmission maxima and broader peak, is mainly due to radiative damping of SPP, that increases with hole size.

## 4.2.2 Effect of Lattice Period

Periodicity is very important parameter in determining peak position. The contribution of lattice period on the transmission spectrum can be interpreted from equation 4.2. It can be observed in the following Fig 4.3.Transmission peak gets redshifted when periodicity is increased and also normalized transmission decreases. A transmission minimum can be seen nearly fixed at a wavelength that is equal to the period of the square lattice, $\Lambda$.
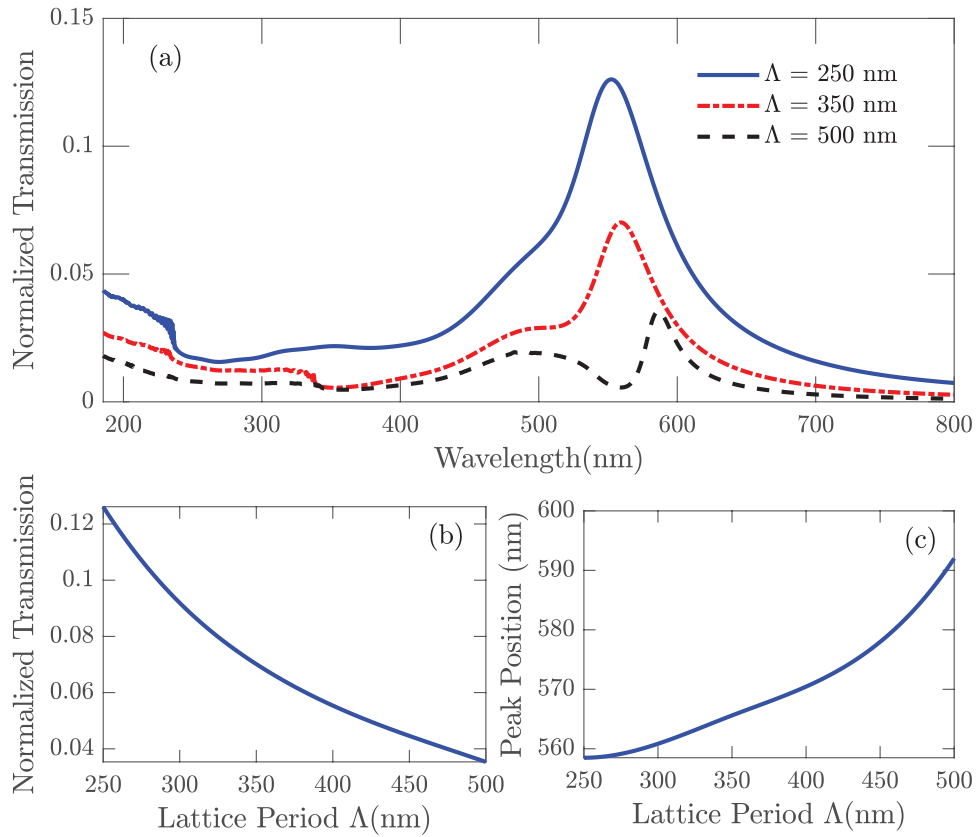
Figure 4.3: (a) EOT spectrum for different lattice periods of the nano-hole array comprised of square holes with side length $d_h$= 100 nm. A closer look reveals the minima of the spectra changing with the periodicity of the lattice. (b) A decrease in the transmission spectra with increasing lattice period. (c) Red shifting behavior of the transmission peak with increase in period length.

## 4.2.3 Effect of Hole shape and film Thickness

Before, research on the influence of hole shape on EOT through periodic hole arrays,[71] structures producing EOT consisted of circular hole arrays. Changing the shape from circular to rectangular caused not only an increase in the transmission spectrum, but caused a red shift in the peaks. Figure 4.4 shows the EOT spectra for a gold (Au) nano-hole array comprised of square holes and circular holes. The period of the array, $\Lambda$ was set at 250 nm and film thickness, $t_h$ was 100 nm. Spectral position of transmission peak remains the same irrespective of the thickness of metal film. But width of the peak changes with thickness. It was seen that width is depended on the aspect ratio (thickness/hole width ratio).[69,72] The larger the ratio is the less the width of the peak can be seen. Peak gets broadened when this ratio is decreased. Behaviour of the transmission modes for variation of different parameters has been exploited to generate dual-mode response. The findings regarding EOT characteristics that have been studied and observed can be summarized as:

- Hole periodicity determines spectral peak position.

- As hole dimension increases so does transmission spectrum

- Hole shape strongly influences transmission spectrum.

- Aspect ratio ($t_h/d_h$ ratio) strongly influences the peak bandwidth
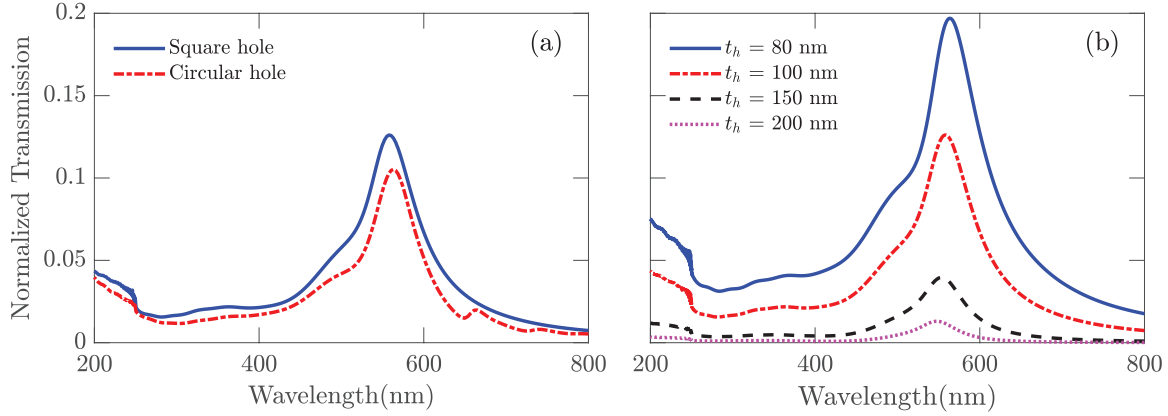
Figure 4.4: (a) EOT spectra observed for a simulated nano-hole array with period, $\Lambda = 250$ nm, and hole width, $d_h = 100$ nm. For both kind of holes, a sharp dip at around 250 nm leading upto the transmission minimum is observed. (b) Transmission spectra for a NHA having hole period 250 nm, hole width 100 nm, and different film thickness $t_h$.

## 4.3  Exploring concepts: Optical Tamm States

Like Surface Plasmon Polariton (SPP), Optical Tamm state (OTS) is also a surface wave. OTS exists at the interface between a metal and a Distributed Bragg reflector (DBR).[73] It can also be seen at the interface between two DBRs. A DBR is a 1D Photonic Crystal with a wide photonic energy bandgap. Tamm state was first demonstrated as electron states,[74] at crystal structure termination. It occurred in energy band-gap at crystal surface. OTS at the photonic band-edge are the photonic counterparts, of the electronic Tamm states.

The wisdom behind choosing OTS instead of SPP resonance, is to circumvent the limitations of SPP excitation. Normal incident light on plane metal-dielectric surface is not sufficient for SPP excitation, as SPP has a large momentum that can't be matched through normally incident light on plane surface. To excite surface plasmons, diffraction gratings or prisms are needed to match the momentum. And moreover, polarization of incident light also plays a significant role as only TM polarized light can generate SPP. The decay of SPP in metal and dielectric occur due to negative dielectric coefficient of metal and total internal reflection respectively. From the dispersion relation of SPP we find that, the dispersion curve lies to the right of the light line given by $k_0 = \omega/c$, where $k_0$ is the in plane wavevector of light. That's why simple optical excitations in planar structures can't generate SPP.

However, Tamm plasmons are surface EM field localizations at the boundary of periodic atomic potential. OTS can be generated through both TE and TM polarization of incident light and it does not need any grating surface for momentum matching. OTS has zero in plane wave vector and can be generated through direct optical excitation. Dispersion relation of Tamm plasmon lies to the left of the light line, $k_0 = \omega/c$. So, normal excitation is possible. The decay of Tamm plasmons in metal due to negative dielectric coefficient, is much shorter than the decay in dielectric, which occurs due to the stopband in photonic crystal. In our cavity design, Tamm Plasmons offer the required resonance for cavity design.

**States at DBR-Metal interface**
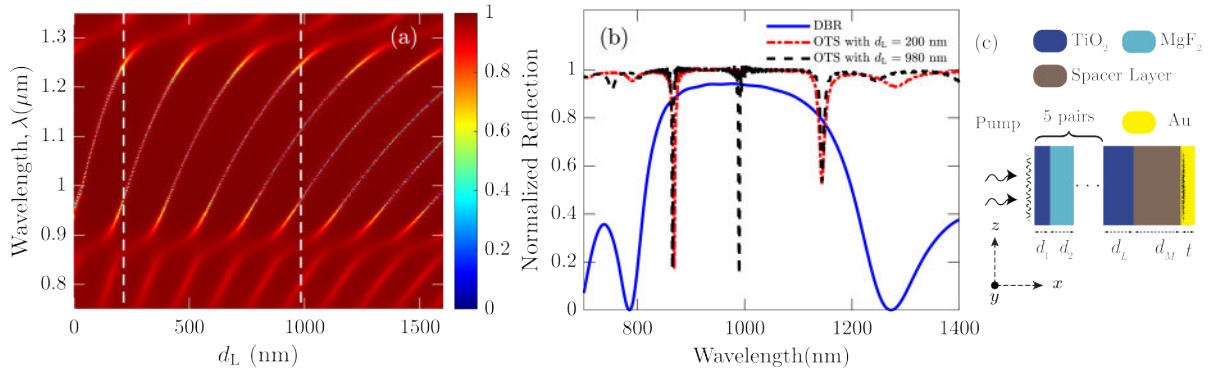


Figure 4.5: (a) Normalized reflection spectra for varying final layer thickness$d_L$ for metal thickness, t=100 nm. The white vertical dashed lines at 215 nm and 980 nm, indicate the onset dual and triple optical Tamm states respectively within the photonic band-gap (PBG) of the DBR. (b) The reflection spectra for two different $d_L$ shown along with the DBR reflection spectra. (c) Schematic of the simulated cavity.

OTS in a DBR-metal interface has been observed for the DBR in Fig. 4.5. In this structure TiO$_2$ layer width is $d_1 = 109$ nm, MgF$_2$ layer width is $d_2 = 165$ nm, PU spacer layer thickness is $d_M = 325$ nm and terminating TiO$_2$ layer width is $d_L$ is varied. When an Au thin film is interfaced with a DBR, we observe OTS at the metal-DBR interface. This state can be coupled with SPP.[75] Thus, in a perforated film, existing EOT modes can be further amplified by the use of DBRs. We can tune the position of the OTS mode by changing $d_L$. The spectral distance between the two OTS modes can be controlled by changing the thickness of the final TiO$_2$ layer ,$d_L$.[76] Thus, one possible way of producing visible dual-mode lasing can be, by bringing the two resonances closer together within the envelope of the gain medium lasing linewidth. To that end, on increasing $d_L$, the spectral distance between the modes decrease. Fig. 4.5 shows that, for a $d_L$ of 980 nm, 3 modes appear within the bandgap of the DBR. However, for increasing final TiO$_2$ layer length, the field profile at the region just adjacent to the metal interface can become significantly attenuated, which would ultimately affect lasing performance. So, this is not a successful approach to produce dual-mode lasing. But, this phenomenon of being able to change OTS position with the thickess of a single layer, is very handy for tuning the lasing mode, as it is seen in the next chapter.

## 4.4   Cavity design I: Merged Lattice NHA in Metal Film.

So far, the lattice structure suggested for EOT via nano-hole array produces single mode output and is dominated by individual hole resonances. The dimensions chosen primarily for determination of modal characteristics couple energy to only a single mode.

This metal-NHA doesn't generate dual-mode transmission spectrum. a periodic arrangement of holes on thin Au film results in an enhanced transmission spectrum as observed from section 4.2. A simple nano-hole array produces single-mode output with emission wavelength determined by individual hole resonances. This phenomenon can be exploited with careful optimization, in designing a plasmonic cavity that produces dual transmission modes. The periodicity of nano-holes and the dimension of individual holes and degree of coupling of LSPs at neighbouring holes change the resonances, and hence, the
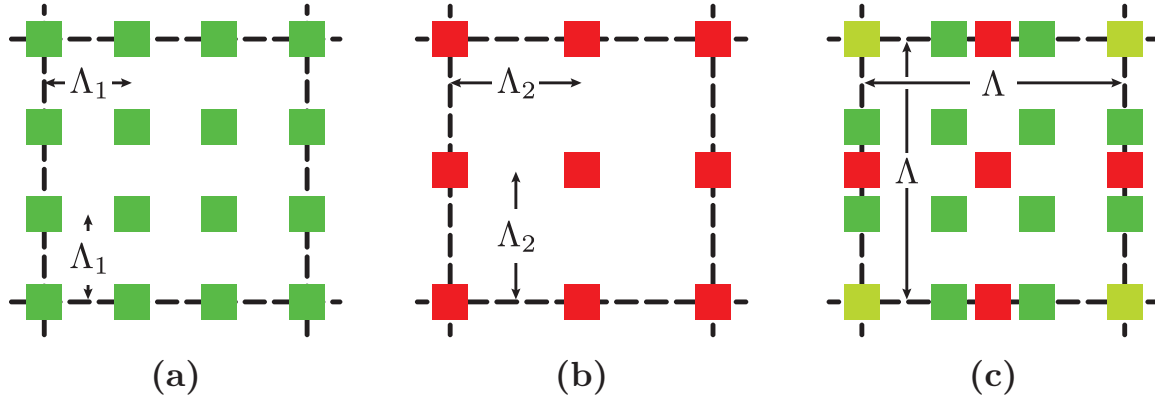
Figure 4.6: Merging of two square lattices of periods $\Lambda_1 = 250$ nm (a) and $\Lambda_2 = r \times \Lambda_1 = 375$ nm (b), where, $r = R/(R-1)$, and $R$ is an integer greater than 2. (c) Only $R = 3$ gives satisfactory dual-mode response. Other values do not generate multiple modes.

emission spectrum.[71,77] However, the desired dual-mode response can be achieved by utilizing some of the features of the EOT spectra produced by a combination of these simple metal-NHAs. Since the periodicity of the nano-holes affect the mode position, incorporating twofold periodicity in the Au-NHA was the viable option. Also, theoretical works on how to merge two slightly different 2D lattices in a regular pattern was reported by Alagappan et. al.[78]

In the metal layer, we have superposed square hole array with two different periodicity, as shown in Fig. 4.6. The square holes have a dimension of 100 nm $\times$ 100 nm. In the densely placed square hole array, the hole periodicity ($\Lambda_1$) is 250 nm, as shown in Fig. 4.6(a). By contrast, in the sparsely placed square hole array, the hole periodicity ($\Lambda_2$) is 375 nm, as shown in Fig. 4.6(b). In both NHA, four corners have identical square holes. In our proposed structure, the two square hole arrays are merged keeping them concentric, so that the merged lattice becomes a square with a periodicity ($\Lambda$) of 750 nm in both the $y$- and $z$-directions, as shown in Fig. 4.6(c). The holes at the four corners of the merged lattice - indicated by light green, is a common overlap from both the sparsely and densely placed NHAs. It was also observed that only square nano-holes arranged as per the mentioned periodicity, showed dual-mode response. Au-NHA with circular nano-holes or square nano-holes with any other periodicity arrangement did not show dual-mode spectrum.

In Fig. 4.7, the transmission spectra through the simple NHAs and the designed merged lattice NHA are shown. The simple NHA produces a single transmission peak, as expected. However, the designed merged lattice NHA results in not only an enhanced transmission through the metal layer, but also localization of light intensity in more than one modes.[79] The individual modes of the NHAs, which have been merged, show transmission peaks at 558 nm in Fig. 4.7(a) and 570 nm in Fig. 4.7(b). We show the transmission spectra of the our designed merged lattice NHA in Fig. 4.7(c). The periodicity of a unit cell of the merged lattice is a common multiple of the individual short-scale periods ($\Lambda_1 = 250$ nm and $\Lambda_2 = 375$ nm). The dual-mode lasing is very sensitive to the hole and period parameters of the metal NHA. Change in the periodicity and hole width size of the NHA had to be designed carefully, otherwise the dual-mode lasing might cease to exist, because of not being supported by the gain medium linewidth. Thus, the period span and the hole size had to be optimized in such a way that the cavity mode is supported by the linewidth ($870 \pm 50$ nm) of the gain medium. Also, the ratio of the two short-scale periods had to be $r = 3/2$.
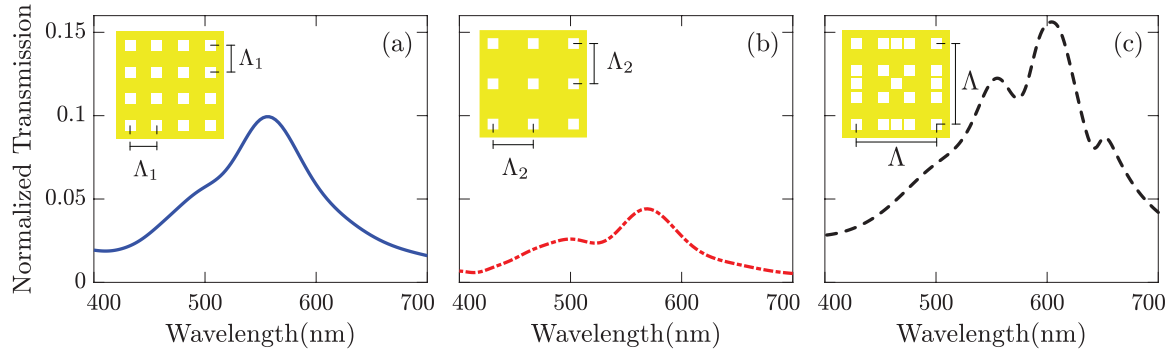
Figure 4.7: (a), (b) Normalized Transmission of bare metal NHA etched with a simple square lattice of period 250 nm and 375 nm respectively. (Au nano-hole array schematic shown in inset)(c) Normalized Transmission of bare metal NHA etched with a Merged lattice of period 750 nm. The EOT shown here is similar to that in the simple lattice, except with more pronounced dual peaks. Overall transmission has also increased compared to simple sqaure lattice.

For the combined complex NHA as shown in Fig. 4.7(c)-inset, the combined period of the unit cell was $\Lambda = 750$ nm.

The merged lattice nano-hole array for this structure incorporates better localization than a simple periodic system. Such merging causes disruption of the periodic pattern in the short spatial scale. This aggregates a large number of scattering loops of light waves and causes a variety of light localization states. Such an arrangement of holes in the array would have a degree of randomness in the short scale. Random systems, relying on scattering, have produced lasing in random lasers. In disordered systems, quantum reflections occur, that make wavefunction halt. Anderson theorized that when sufficient randomness is introduced in such systems, transport can be limited and localized.[80] The naturally occurring cavity resonance due to randomness offered by Anderson localization regimes have been utilized to produce strongly confined nano-lasing in.[81] Increased localization of waves directly results in a better cavity design for multimode laser as it provides necessary optical feedback, in more than one modes, for entrapping light.

This concept has been extrapolated in designing this merged lattice nano-hole array etch. Such an arrangement is actually pseudo-random in nature, as there is randomness in the short scale, but a fixed arrangement in the longer scale. The simple lattices have been chosen such that they differ slightly in spatial resonance which coalesce together to form 2D spatial beats.[78] Thus, localization of waves in such a merged lattice NHA, generate two modes. It was also observed that only square nano-holes arranged as per the mentioned periodicity, showed dual-mode response. Au-NHA with circular nano-holes or square nano-holes with any other periodicity arrangement did not show dual-mode spectrum.

**Resonances of the optical cavity**

To enhance the transmitted modes by the merged lattice NHA, we add a DBR (i.e. 1D PhC) on the top of the PU layer. This forms the passive optical cavity structure of a laser. The OTS at the Au-PU interface couples with the EOT modes. The passive optical cavity's transmission spectra for a broad-band incident
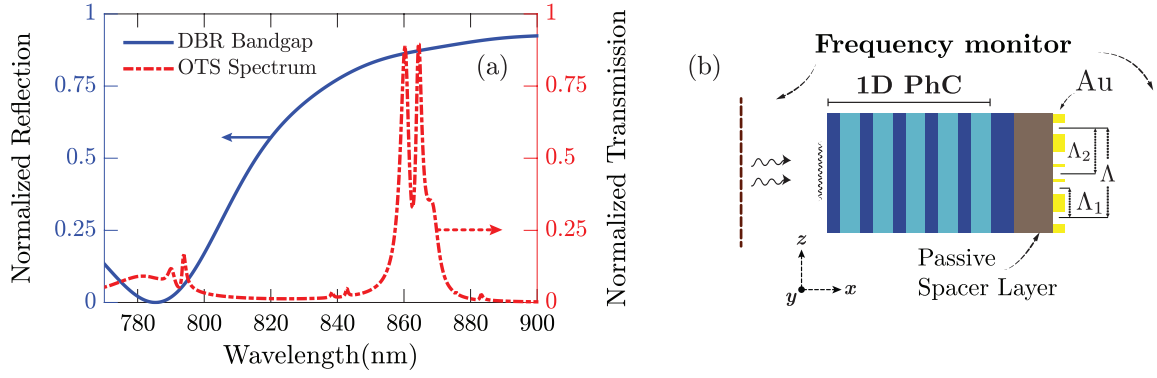
Figure 4.8: (a) Normalized Reflection spectra of just the bare 1D Photonic Crystal - DBR (blue curve), showing only the first band edge. The transmission spectrum of the final bare cavity - shown in (b) - splits into two modes (red curve). The splitting occurs, due to the incorporation of the merged lattice (ML) structure of the metal NHA. The two different peaks correspond to the two different surface Tamm states due to the two periodicities that make up the merged lattice metal NHA. (b) The structure and the simulation setup for obtaining the bare cavity spectral response.

pump is shown in Fig. 4.8. We find that the EOT modes from the isolated merged lattice metal layer has been red-shifted from that presented in Fig. 4.7(c). In particular, the transmission spectra have peaks at 865 nm and 870 nm. We also note that the inclusion of PhC on top of PU spacer layer enhances the transmission intensity. The transmission spectra of the cavity with a passive medium, instead of the gain dye molecules, is plotted against the backdrop of a bare DBR reflection spectra.

Presence of the periodic potential variation in the DBR, excited the Tamm plasmons on the metal-PhC interface, which enhances the extraordinary transmission from the nano-holes.[82]

To ensure proper cavity response for the design, the OTS resonance was regulated to be around 870 nm for maximum gain. As band edge states offer higher quality response and better wave localization,[51] the DBR has been regulated to have its first band edge at the position of the OTS mode, at around 870 nm. To that end, the transmission spectra of the cavity with a passive medium, instead of the gain medium, is plotted against the backdrop of a bare DBR reflection spectra (Fig. 4.8).

## 4.5   Cavity design II: Linear Asymmetric DBR pair.

Our gain medium, the IR-140 dye peaks at $\sim 870$ nm and has a gain lineshape of 100 nm. To ensure a proper dual-mode cavity response for the design, the OTS resonance needs to be regulated at around 870 nm for maximum gain. The OTS peaks occur within the photonic bandgap (PBG)/ photonic stop band of the DBR. So, the OTS mode is regulated to be at the position of the first band edge of the DBR, because band edge states offer higher quality response and offer better wave localization.[51]

**Photonic Bandgap Engineering**

DBRs show photonic bandgap in their spectra with no reflection minima within the bandgap region. This wide photonic bandgap spectra can be used to control the properties of light. We have cascaded two DBRs of the same material pair in our structure. To that end, a DBR composed of alternating layers of $TiO_2$ and $MgF_2$, each having an index of 2.23 and 1.46 was utilized. The alternating layers of $TiO_2 - MgF_2$
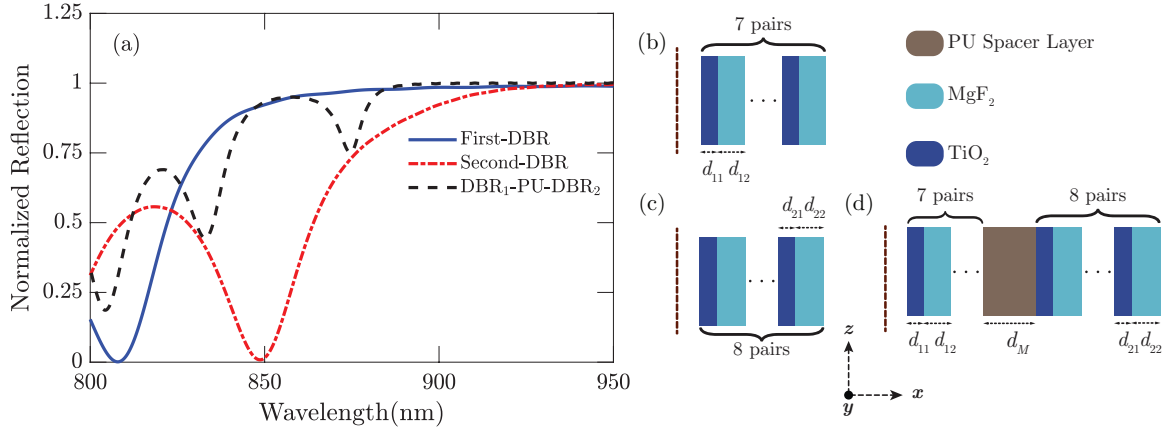
Figure 4.9: (a) Normalized Reflection spectra for separate PhCs - first-DBR (blue solid), second-DBR (red-dash-dot) and when two DBRs are cascaded (black). The first photonic band edge is shown. (b-d) The schematic of the respective structures structure, whose reflection spectra are plotted in (a). (c) The cascading of two DBRs.

pair acts as a photonic bandgap crystal which produces the PBG stretching from $\sim 870$ nm to $\sim 1200$nm. In this structure, $TiO_2$ layer width is $d_{11} = d_{21} = 109$ nm, $MgF_2$ layer width is $d_{12} = 165$ nm for the first DBR and $d_{22} = 180$ nm for the second DBR. Terminating $TiO_2$ layer width is $d_L = 210$ nm and PU spacer layer thickness is $d_M = 325$ nm. Also if another DBR - composed of the same material pair, but of slightly different thicknesses - is cascaded on top of the passive PU layer, OTS at the photonic bandedge is observed.[83] In such a case, as evident from Fig. 4.9, the DBRs are designed in such a way that they offer slightly different bandgap regions when analysed individually. Bandgap of separate DBRs fit into the range of bandgap of the two DBRs cascaded. Two reflection minima can be seen in the bandgap of Linear asymmetric DBR pair scheme. Fig. 4.9 clearly shows that optical resonance is generated by using two 1D DBRs (dashed black line in figure) connected by a spacer layer.
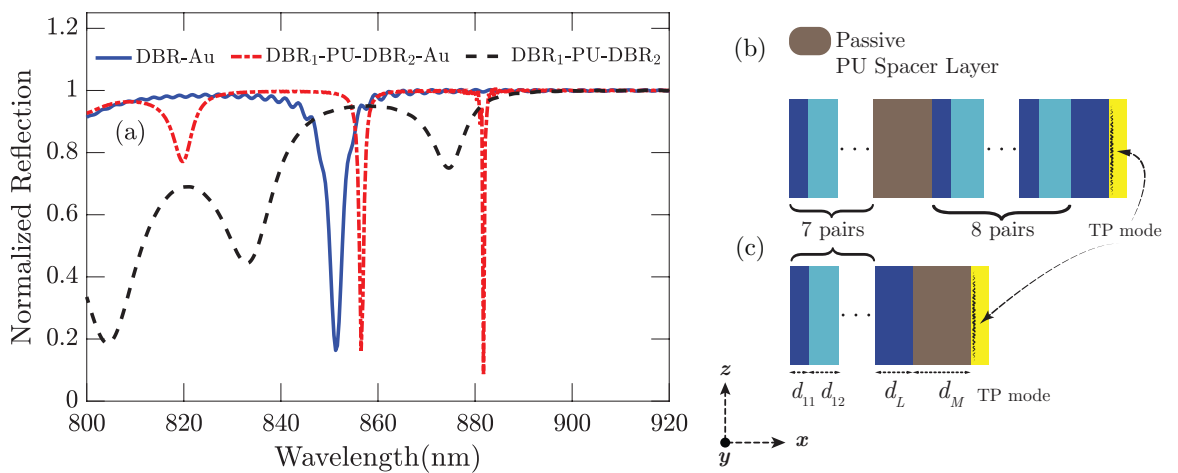


Figure 4.10: (a) The reflection spectra of the structure in (b - red curve) and (c- blue curve) on top the reflection spectra (black dashed curve) of the structure in Fig. 4.9(d). (b) The ($DBR_1$-PU(Polyurethane)-$DBR_2$-Au) structure, whose spectrum (red curve) is plotted in (a). (c) The cascaded $DBR_1$-PU(Polyurethane)-Au structure.

## Resonances of the optical cavity

Further coupling these modes to plasmonic mode at the metal interface, introduces a new term that can effectively reduce the confinement of the mode within subwavelength dimensions. We terminated the structure by adding a metal layer. This metal layer helps to incorporate plasmonic effects in the cavity mechanism. Fig. 4.10 shows, that a single DBR terminated by a metal layer, exhibits only one reflection minima in the photonic bandgap region. This is the Optical Tamm State. However, using two DBRs back to back with a noble metal layer - Au - generates two distinct reflection minima. Two DBRs are cascaded as shown in Fig. 4.9(d) and addition of metal layer gives rise to two reflection minima in the PBG of the cascaded DBRs. Incorporation of multiple interface states have contributed to create the two reflection minimas. One of the resonance corresponds to the OTS resonance at DBR-Au junction. Fig. 4.10(a) shows that one of the resonance corresponds to the OTS resonance at DBR-Au junction. This is further proven, by the fact that, the mode shifts its wavelength when $d_L$ is changed. The other resonance is caused by the OTS between the two stacked DBRs at the gain medium. The two DBRs are not identical. As the two DBRs are slightly different, defect mode is obtained at their junction. The $MgF_2$ layer thickness is different for the two DBRs, as mentioned in Fig. 4.9. Also, the second DBR has 8 pairs of $TiO_2 - MgF_2$ layers as opposed to 7 pairs of the first DBR. Hence, these two DBRs are asymmetric. As the two DBRs are slightly different, defect mode is obtained at their junction.

In the given resonator structure, it is these Tamm plasmon states which build up the energy for lasing action when the active medium is incorporated. When succeeded by a metal layer, additional Tamm Plasmon Polariton (TPP) states are formed at the metal interface facing the crystal.

# Chapter 5

# Analysis of Devised Dual-Mode laser

After going through the process of developing a proper plasmonic-photonic cavity, we tested the cavity performace, as a component of a plasmonic laser system. The physics and features of the cavity, two cavity designs producing lasing modes were introduced. In the end, there were two distinct cavity structures, which could produce dual-mode lasing. Both the structures utilized Extraordinary Optical Transmission (EOT) and Optical Tamm state (OTS) resonances. In one design, EOT resonances at two different wavelengths, were combined to generate two hybrid plasmonic modes. In the other design, two hybrid Tamm states gave rise to two modes. The two structures that have been analyzed showed dual-mode transmission spectrum, in the 850 to 900 nm range. This chapter is devoted to the performance analysis and possible tuning capabilities of the two devised structures.

Having explored two variants of the cavity design, we further simulated the response of both these structures incorporating a gain medium. In both cases, as we used the same IR-140 dye molecules doped in Poly-urethane gain medium. Both the structures have been simulated using similar conditions and environment in Lumerical FDTD Solver. The structure was optically pumped using a 800 nm planewave pulse of 40 fs pulse length along $x$-direction, with $E$-field oscillating along $z$ direction. Both of our structures are periodic along the $y$ and $z$ axis. Thus, the simulation region contained a unit cell along $y$ and $z$ direction. As the structure was symmetric along both axes, symmetric and anti-symmetric boundary conditions were used along $y$ and $z$ axis. Along the direction of wave propagation, i.e along $x$-axis, PML boundary conditions were used. For the perfectly matched layer boundary condition, we used uniaxial anisotropic PML along the $z$-axis.

## 5.1   Design I: Merged Lattice Plasmonic Laser

The proposed merged lattice plasmonic laser structure is shown in Fig 5.1. At the core of the proposed plasmonic laser's optical cavity, the gain medium consists of IR-140 dye molecules embedded in polyurethane (PU) matrix. The parameters of this gain medium is tabulated in Table 3.1. The dye molecules offer
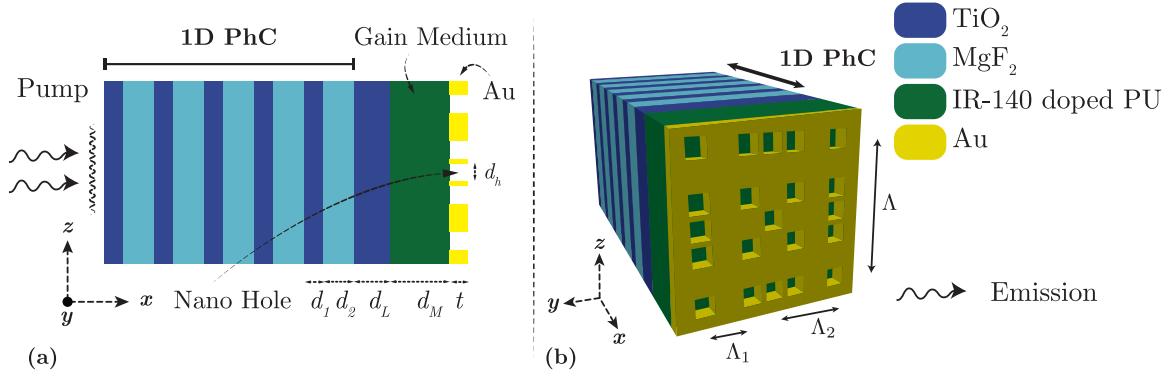
Figure 5.1: (a) Schematic diagram of a longitudinal section across the structure. In the diagram $TiO_2$ layer width $d_1 = 109$ nm, $MgF_2$ layer width $d_2 = 165$ nm, last $TiO_2$ layer width $d_L = 200$ nm, gain medium thickness $d_M = 325$ nm and metal NHA thickness $t = 100$ nm. In the merged lattice NHA structure, the two periods are $\Lambda_1 = 250$ nm, $\Lambda_2 = 375$ nm. Overall, the unit cell has a period of $\Lambda = 750$ nm. The hole width is $d_h = 100$ nm for all the nano-holes. (b) The 3D schematic of the structure. All components have been drawn to actual scale.

gain to the incident pump energy. On one side of the gain medium, opposite to the optical pump, a 100-nm-thick Au film is perforated with nano-holes. On the other side, there is a 1D photonic crystal made up of alternating layers of $TiO_2$ and $MgF_2$. We use the refractive index of $TiO_2$ and $MgF_2$ to be 2.23 and 1.46, respectively. Unless stated otherwise, we assume that the structure contains five pairs of $TiO_2$-$MgF_2$ layers.

In the metal layer, we have superposed square hole array with two different periodicity, as shown in Fig. 4.6. The parameters of the NHA have already been explained.

## 5.1.1 Dual-mode lasing Demonstration

In Fig. 5.2a, we show the lasing emission spectra of the designed structure when the polyurethane layer is doped with IR-140 dye molecules. We note that the emission occurs at two isolated modes with peaks at 870 nm and 878 nm. The resonance can be attributed to two distinct surface plasmon modes localized at the nano-holes. The structure showed cavity modes at 865 nm and 870 nm as previously mentioned in Section 4.4. It is seen that the plasmonic lasing modes in Fig. 5.2(a) are slightly red shifted compared to the bare cavity modes in Fig. 4.8(a). This shifting can be explained by understanding the underlying physics of coupling of surface plasmon mode to free wave radiative mode. Surafce plasmon mode line lies below light line in dispersion diagram. Surafce plasmon has higher wavevector compared to free wave. That's why when SPP is coupled to radiative free wave there is a dip in wavevector or in other words can be said that increase in emission wavelength. The gain profile of IR-140 is centered around 870 nm and has linewidth of ~100nm[84] which is wide enough to support both the modes produced. To ensure both of the emission modes are lasing modes we investigated the input vs output characteristics of our designed merged lattice plasmonic laser. Existence of threshold behaviour can prove that lasing is taking place. We varied the amplitude of the incident pump pulse and calculated the lasing emission intensity. The results are given in Fig. 5.2(b).We note that the device does not show lasing emission when the peak electric field of the pump pulse is $< 1.5 \times 10^7$ V/m. However, the output emission intensity increases suddenly at a rapid rate as the pump field reaches $\gtrsim 1.5 \times 10^7$ V/m. We note that the laser emits
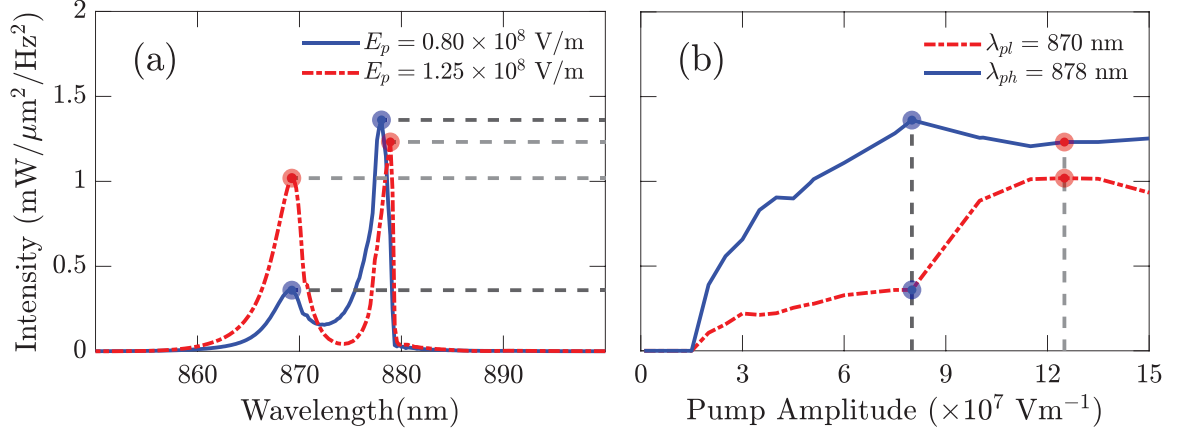
Figure 5.2: (a) Dual-mode lasing emission of the proposed laser structure. The lasing spectrum for a pumping amplitude of $0.80 \times 10^8$ V/m (blue) and $1.25 \times 10^8$ V/m (red) for this particular response is indicated in (a) by the dashed dark and light gray lines respectively. (b) Peak intensity for the two modes versus the pump amplitude.

dual-modes simultaneously after crossing the threshold pump field. Such dependence of output peak emission on input pump power suggests that both modes are lasing modes. Taking the area of the device into account the threshold value of the structure is $1.2 \times 10^{-3}$ mJcm$^{-2}$. It is an order less than reported in the single mode laser in[3] a threshold of $1.3 \times 10^{-2}$ mJcm$^{-2}$.By adding a merged lattice NHA we have been able to reduce threshold for the dual-mode laser over simple periodic NHA laser design in.[3]Better localization thus helped to reduce the threshold value for our laser. Our proposed structure has significant improvement over the existing reported dual-mode laser devices threshold characteristics; 0.16 mJcm$^{-2}$ (simulation) or 0.3 mJcm$^{-2}$ (experimental) for dual-mode plasmonic superlattice based laser structure[51] and 3.3 mJcm$^{-2}$ for Ni nanodisk array based dual-mode plasmonic laser.[52] Such small threshold value can be utilized even in low power device regime. The emission intensities for the smaller and longer wavelengths show similar trends in the transmission side. Above threshold value,at first both of the mode intensity increases with increasing pump amplitude at a high rate. Then after $> 1 \times 10^8$ V/m, this increase is at a slower rate.The longer wavelength has a greater intensity than the smaller wavelength.

## 5.1.2   Spatial Field Distribution

We show electric field profiles in the transverse and vertical cross-sections of the plasmonic laser structure. In the transverse cross-section, i.e., along the metal-gain medium interface, the $\vec{E}$ field profile shows that plasmonic modes are excited at the corner holes at a smaller wavelength of the incident light, as shown in Fig. 5.3(a). By contrast, plasmonic modes are excited at the central holes at a longer wavelength of the incident light spectrum, as shown in Fig. 5.3(b). The incident plane wave was polarized along the $z$-direction, and the modes have been excited perpendicular to that direction. The SPP mode along the hole edge has also been excited. Since the holes are 100 nm in size, the closer holes are only separated by 25 nm. Therefore, LSPs in two neighboring holes across such a small distance couple and form stronger modes. In Figs. 5.3(c) and (d), we show electric field profiles in the vertical cross-section along the center of the unit cell at a light wavelength of 869 nm and 879 nm, respectively.
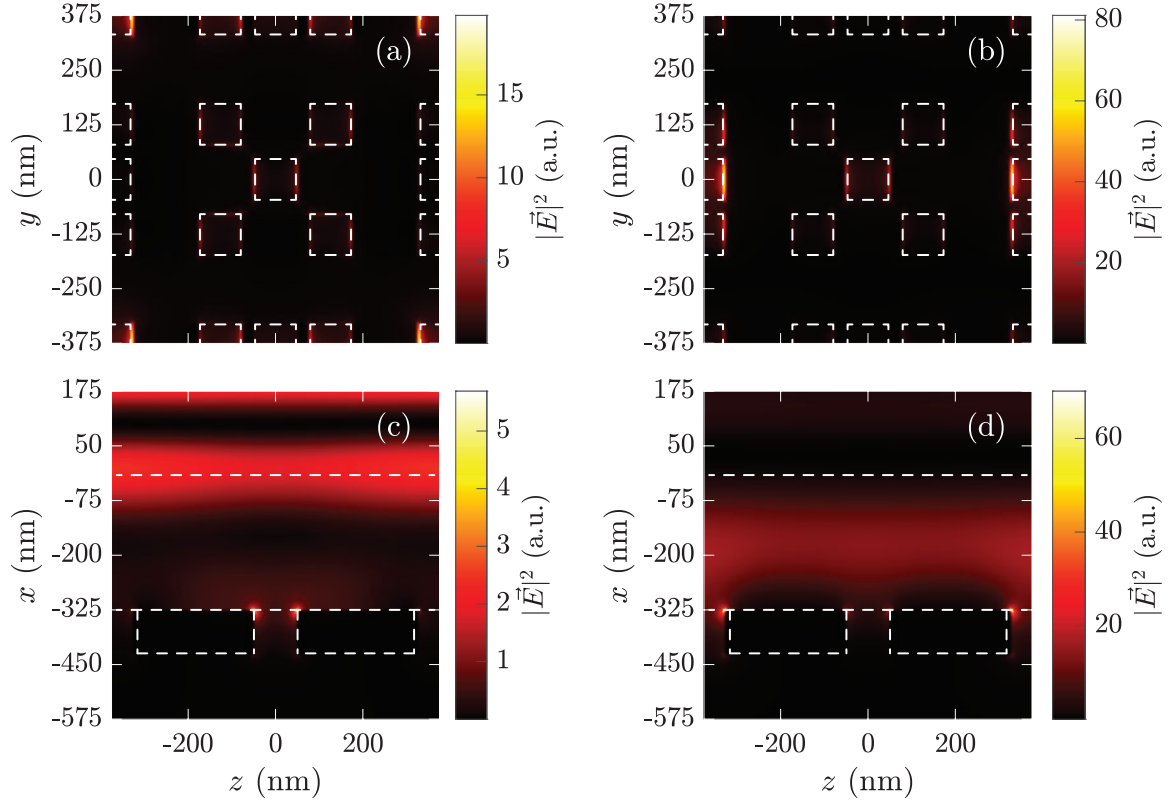
Figure 5.3: (a)-(b): The transverse section (TS) $\vec{E}$-field intensity profile of the structure taken along the metal-gain medium interface. (c)-(d): The longitudinal section (LS) taken along $y = 0$ nm shows $\vec{E}$-field intensity profile of the merged lattice structure. (a),(c): $|\vec{E}|^2$ intensity profile for $\lambda_p = 869$ nm. (b),(d): $|\vec{E}|^2$ intensity profile for $\lambda_p = 879$ nm.

### 5.1.3 Lasing Emission Dynamics

**Near-field Mode dynamics**

To explore the characteristics of the dual-modes we carried out parameter sweep of the proposed device to demonstrate how the emission responds to change. We simulated the structure by varying the number of TiO$_2$-MgF$_2$ pairs ($N$) and the final TiO$_2$ layer thickness ($d_L$) in the DBR photonic crystal. The results are given in Fig 5.4 and 5.5. We find that both the emission wavelength and the intensity of the lasing modes significantly change with the change in $N$ and $d_L$. Because of complex geometry of the merged lattice NHA and mode competition between the dual emissions the output behaviour is non linear.

The final TiO$_2$ layer of the DBR acts as a tuning layer for the proposed laser. It can be used to shift the peak emission wavelength of the dual-modes and their separation. By increasing $d_L$, both the modes are red-shifted and the separation between them decreases, as presented in Fig 5.4.In Fig 5.4(c),(d),(e) by changing thickness from 190 nm to 210 nm the proposed structure can be tuned to emit in lower wavelength mode in a range of ∼859 nm to ∼880 nm. The higher wavelength mode can be tuned in a range of ∼866 nm to ∼885 nm. This gives a wide tuning range for both of the modes.The mode separation taken as the difference between peak wavelength of the dual-modes decreases when final TiO$_2$ layer of the DBR is increased or DBR pair number is increased. A maximum mode separation of 13.4nm was achieved for $N = 9$ with final TiO$_2$ layer 180nm thickness from Fig 5.4(b).
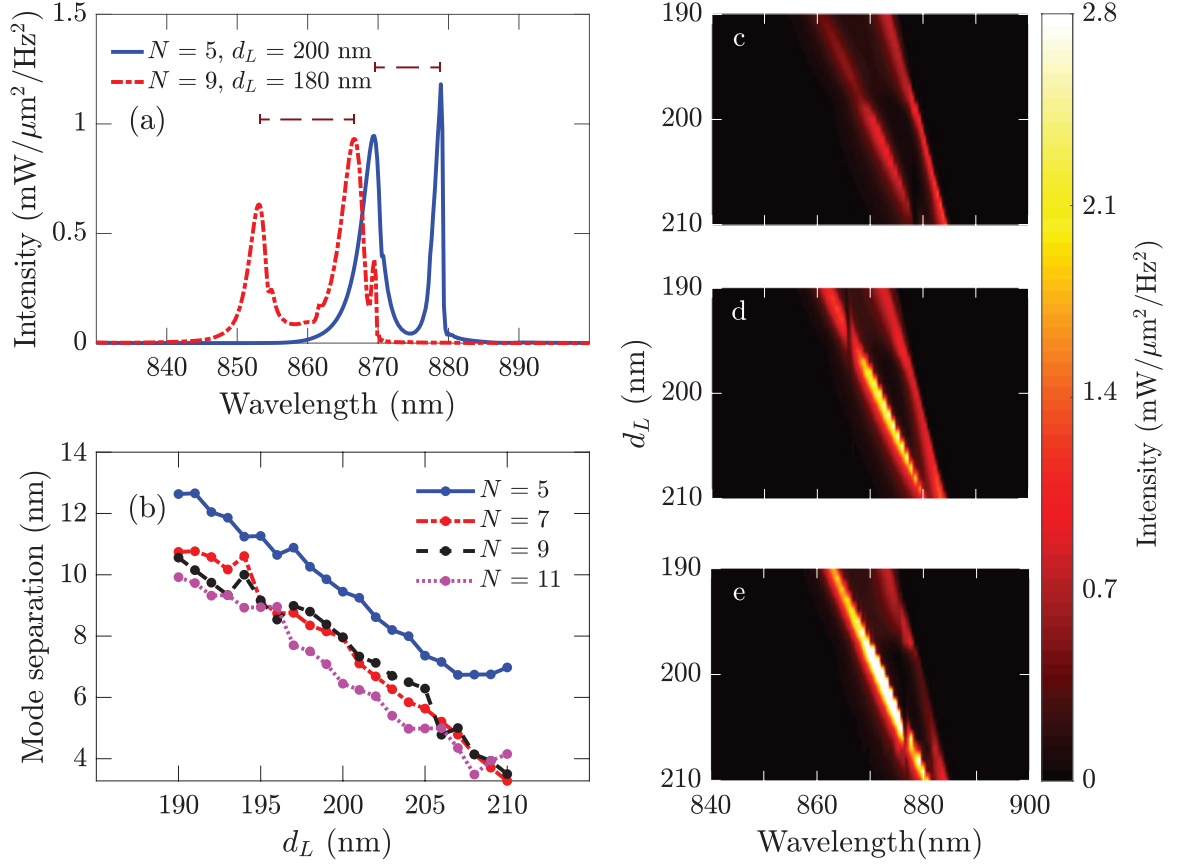
Figure 5.4: (a) Emission intensity spectrum plotted for two different configuration of DBR layer number ($N$) and the terminating $TiO_2$ layer width ($d_L$); ($N = 5$, $d_L = 200$ nm (blue)) and ($N = 9$, $d_L = 180$ nm (red)). The mode separation and the full width at half maximum (FWHM) for both the peaks is indicated. The plot shows shifting of peak emission wavelength. (b) The mode separation of the two dual peaks is plotted as a function of ($d_L$) for different $N$ values. The surface plots on the right column, shows how emission intensity red shifts and varies with $d_L$ for (c) $N = 5$,(d) $N = 6$ and (e) $N = 9$.

The linewidth (FWHM) of the modes show somewhat interesting phenomena as presented in 5.5 (a),(b).Below DBR pair number $N = 7$ the higher wavelength mode has narrow linewidth compared to the lower wavelength mode. As $N$ is increased, it favors the filtering effect of the lower wavelength mode making it more precise and narrow down and the higher wavelength mode linewidth increases.Increasing final $TiO_2$ layer thickness of the DBR responds in narrowing effect on linewidth for both modes.

In a general sense the peak intensity for the lower wavelength mode shows an increasing trend when we increase DBR pair number in Fig 5.5(c). The lower wavelength mode gets favoured by the cavity and thus has more power than the higher wavelength mode when DBR pair is increased. The higher wavelength mode changes from 0.5 mW/$\mu$m$^2$/Hz$^2$ to 2 mW/$\mu$m$^2$/Hz$^2$ as showed in Fig 5.5(d). Increasing the DBR pair thus makes the shorter wavelength mode more prominent. As a result, the longer wavelength mode becomes less dominant when compared to the intensity of the shorter mode. In order to get comparable power in both of the emission modes DBR pairs can be chosen between $N = 5$ to $N = 7$ and Final $TiO_2$ layer thickness can be selected to tune for a wide range from 190 nm to 210 nm. The cavity cannot support dual-modes when $d_L < 180$ nm and $d_L > 220$ nm. Emission for that range shows only a single mode. For selecting $N \geq 9$, $TiO_2$ thickness range must be kept $\leq 195$nm or $\geq 210$nm to
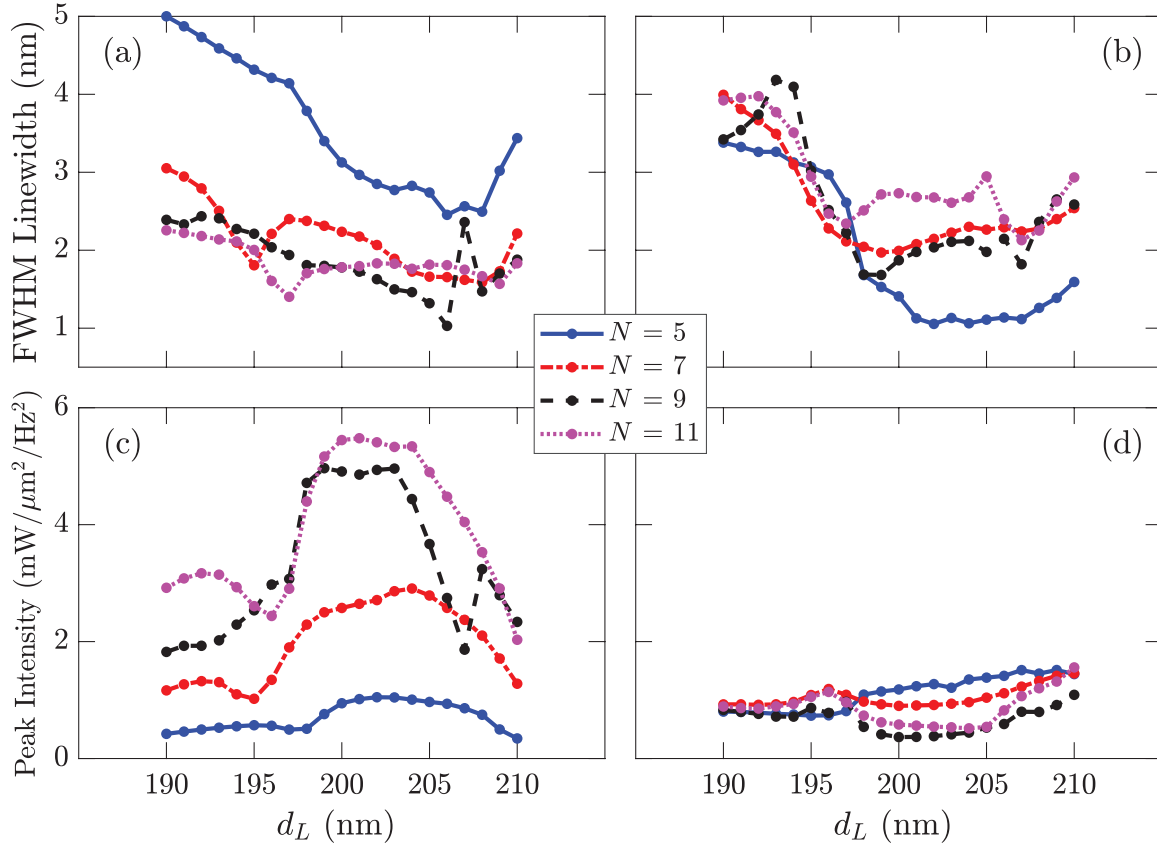
Figure 5.5: (a),(b) The FWHM of the (a) shorter wavelength, $\lambda_{pl}$ mode and (b) longerer wavelength, $\lambda_{ph}$ mode is a function of $d_L$. (c),(d) The Peak emission intensity of the lower wavelength mode (a) and higher wavelength mode (b) is a function of $d_L$. The plots on right column and upper row have the same $y$-axis and $x$-axis as the plots on the left column and bottom row respectively.

keep comparable power in both of the modes.

## Far-field Analysis

One drawback of plasmonic nano laser structures is that, it emits higher order modes in the spatial domain. Reason behind this is the mismatch between wave-vector $(\vec{k})$ of surface plasmon modes and free space propagating modes. Keeping that in mind, we limited the nano-hole periodicity to the subwavelength range. Thus, as the single mode plasmonic laser[3] emitted only zeroth order mode, similar effect is seen for this dual-mode plasmonic laser structure. The LSPs from each of the nano-holes interfere constructively and give us a highly convergent and directional beam. This is because, the patterning of the nano-holes on the Au-NHA is radially symmetric and has twofold periodicity.[85]

An area of 150 $\mu$m$\times$150 $\mu$m along the $yz$-plane of the device was tested for far-field performance. The far-field analysis for both of the modes gave us similar results. The long range periodicity of the lattice and 2 fold symmetry in the ML configuration cause greater constructive interference in the far field. Thus, this laser shows good emission in far field. The far field intensity profile was obtained by projecting the near-field profile to a distance 1m away. The far field FWHM is within a limit of only 0.4° angle which shows significant improvement than other dual-mode lasers.[51,52] It has lower divergence
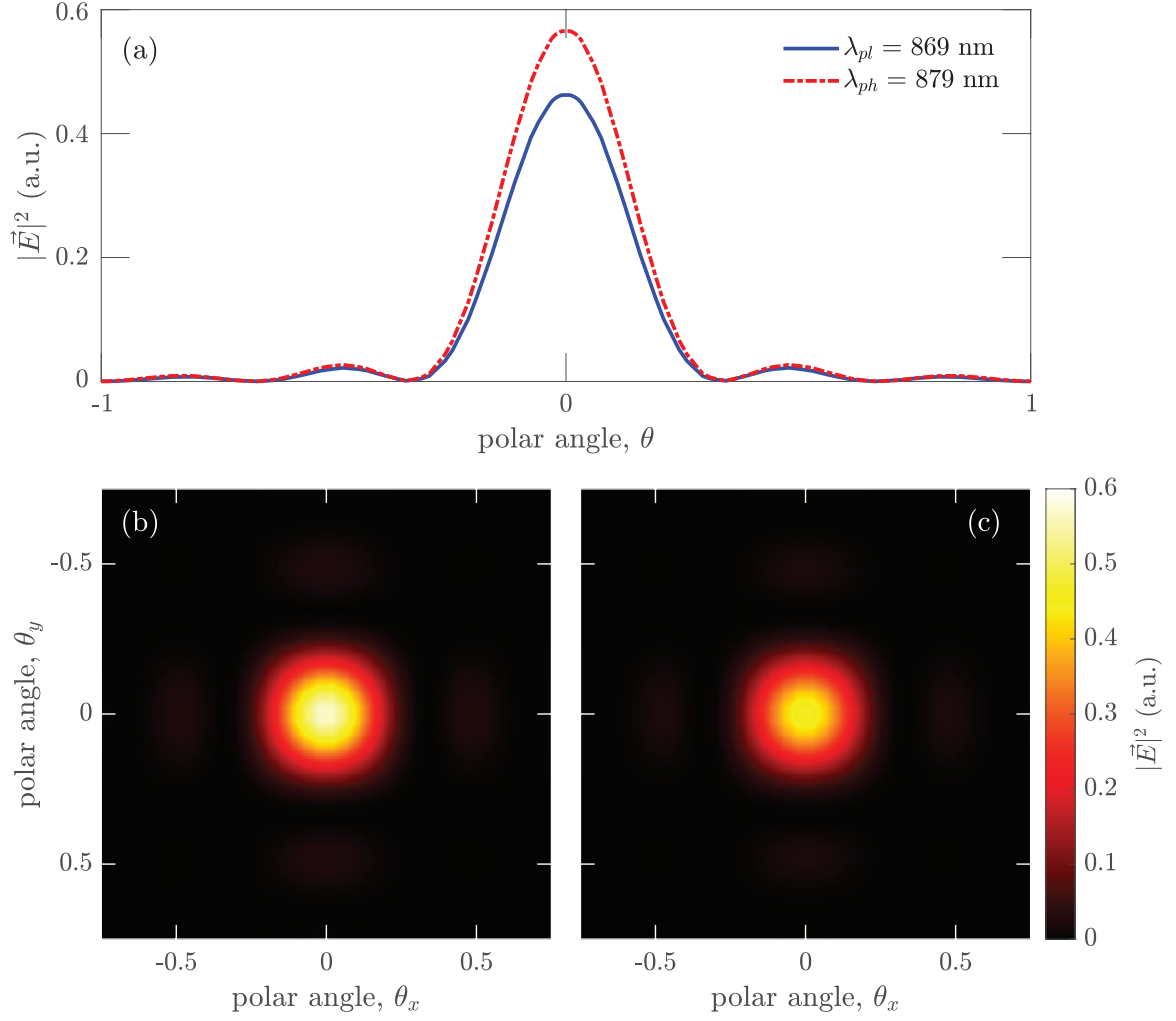
Figure 5.6: (a) far field intensity distribution with respect to polar angle at 0° azimuth. (b,c) Electric field intensity in 2D orientation.

angle than the reported value of $< 1°$ of the single mode laser by Ahmed et. al.[3] So, addition of merged lattice NHA has improved the performance of our dual-mode laser in far field also compared to the single mode laser in[3] and also dual-mode lasers reported by Wang et. al. and Porjamal et. al.[51,52] Our design is thus highly coherent in near-field spatial domain. It can be said that, this dual-mode emission laser has a very high far-field directional behaviour than other dual-mode lasers till date.

## 5.2 Design II: Linear Asymmetric DBR pair plasmonic laser

The other variant of our devised plasmonic laser is depicted in Fig. 5.7. The gain medium is placed at the center of the device structure. The optical cavity consists of two distributed Bragg reflectors (DBRs) placed on the two sides of the gain medium orthogonal to the *x*-direction. At the emission end of the device, opposite to the pump entry side, there is a thin Au planar disk, perforated with $100\,\text{nm} \times 100\,\text{nm}$ square nano-holes with a period of 275 nm. The gain medium slab is a 325 nm thick consisting of IR-140 dye molecules embedded in polyurethane (PU) matrix. The parameters of this gain medium is tabulated in Table 3.1.
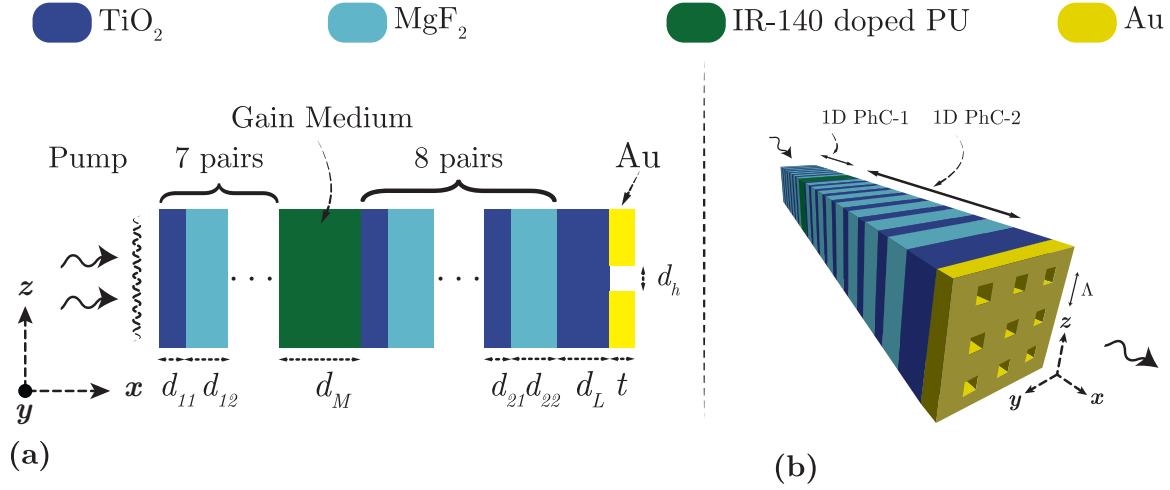
Figure 5.7: (a) Schematic diagram of a longitudinal cross-section of the structure. The parameters in the diagram are TiO$_2$ layer width, $d_{11} = d_{21} = 109$ nm, MgF$_2$ layer width, $d_{12} = 165$ nm for the first DBR and $d_{22} = 180$ nm for the second DBR, terminating TiO$_2$ layer width, $d_L = 210$ nm, gain medium thickness, $d_M = 325$ nm and metal NHA thickness, $t = 100$ nm. In the metal NHA the unit cell has a period of $\Lambda = 275$ nm. (b) The 3D schematic of the structure of the double PhC structure, all components are drawn to actual scale.

The DBRs at the two sides of the gain medium, are 1D PhCs with alternating layers of dispersion-less TiO$_2$ and MgF$_2$, with refractive indices as 2.23 and 1.46. An incident optical pulse, first faces a DBR composed of seven TiO$_2$ − MgF$_2$ layers with thickness of 109 nm and 165 nm respectively. This DBR, preceding the gain medium is hereafter referred to, in this paper as the 'first DBR'. It has 7 pairs of TiO$_2$ − MgF$_2$ layers. Then the pulse arrives at the gain medium, beyond which lies the 'second DBR' composed of eight TiO$_2$ − MgF$_2$ layers, with 109 nm and 180 nm thickness respectively. The first DBR is designed to give a photonic bandgap from 820 nm to 1150 nm approximately. The two DBRs are slightly different. The MgF$_2$ layer thickness in the two DBRs are different. It results in a slightly different photonic bandgap. The second DBR has an additional 210 nm thick terminating TiO$_2$ layer followed by the NHA perforated Au film of 100 nm thickness. The dye molecules offer gain to the incident pump energy.

## 5.2.1 Dual-Mode Lasing Demonstration

The device emits two distinct modes with clear separation as shown in Fig. 5.8. It is also clear from the figure that, without metal NHA the DBR-Gain-DBR structure emits a single mode only. The addition of a terminating metal NHA layer results in dual-mode emission. The pump input versus output emission characteristics of a typical laser system shows threshold behaviour; a knee shape characteristics. The output emission starts to occur rather abruptly once the input pump overcomes the minimum 'threshold' required for lasing emission to occur. This feature is inherent in lasers.[59,60] We find that the threshold is at $4.05 \times 10^7$ V/m pump amplitude. Both of the dual peaks at around 852 nm and 882 nm wavelength shows rising trend; i.e. lasing emission increases with input pump amplitude. Both the peaks show almost equal emission at around $19 \times 10^7$ V/m.
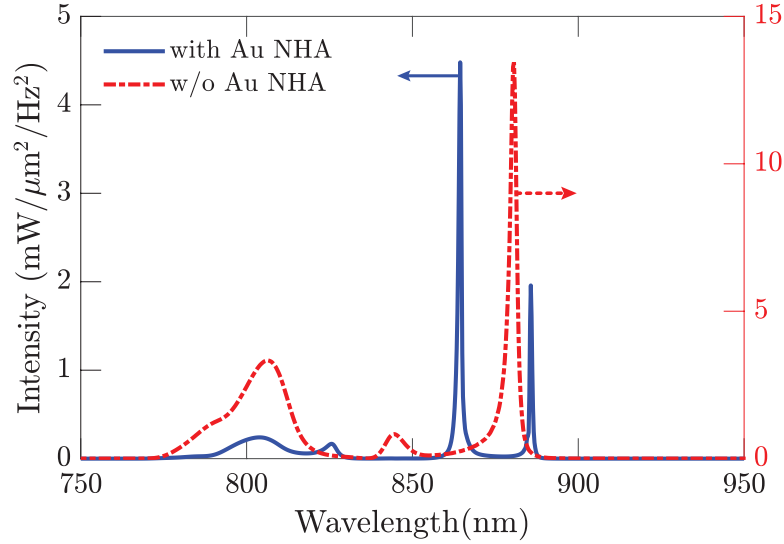
Figure 5.8: Intensity spectra of lasing emission of the structure in Fig. 5.7 - blue curve and in Fig. 4.9(d) - red dash dot curve.
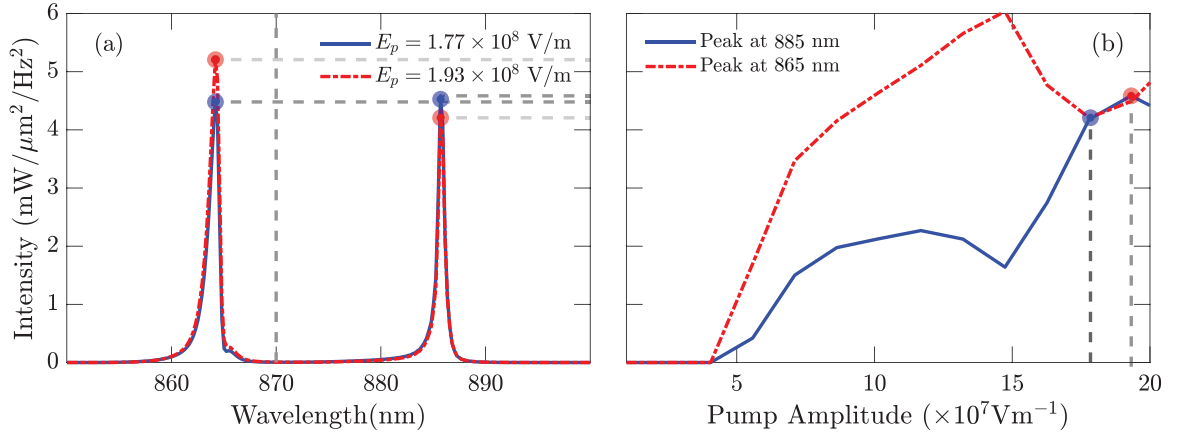


Figure 5.9: (a) Dual-mode lasing emission of the proposed laser structure in Fig. 5.7. The lasing spectrum for a pumping amplitude of $1.77 \times 10^8$ V/m (blue) and $1.93 \times 10^8$ V/m (red) for this particular response is indicated in (a) by the dashed dark and light gray lines respectively. (b) Peak intensity for the two modes versus the pump amplitude.

## 5.2.2 Spatial Field Distribution

The modes at metal dielectric (terminating $TiO_2$ layer) interface has greater attenuation due to the presence of the photonic crystal in between the gain medium and metal. Also, the uniform square lattice NHA produces uniform modal output at given wavelength.

On analysing the field profiles at different cross sections of the structures, we could further delve into the concepts and physics behind the lasing behaviour. It has been possible to identify the resonant modes by observing a real time spatial $\vec{E}$-field distribution. We have designed these structures progressively, after having analysed resonator and laser systems that have already been devised and reported. The cavity was designed in such a way that we obtained two modes in the frequency domain. We have analysed plasmonic mode excitation due to OTS excitation between metal and a 1D photonic crsytal. Also, EOT through the nano-holes seek to enhance those excitations.
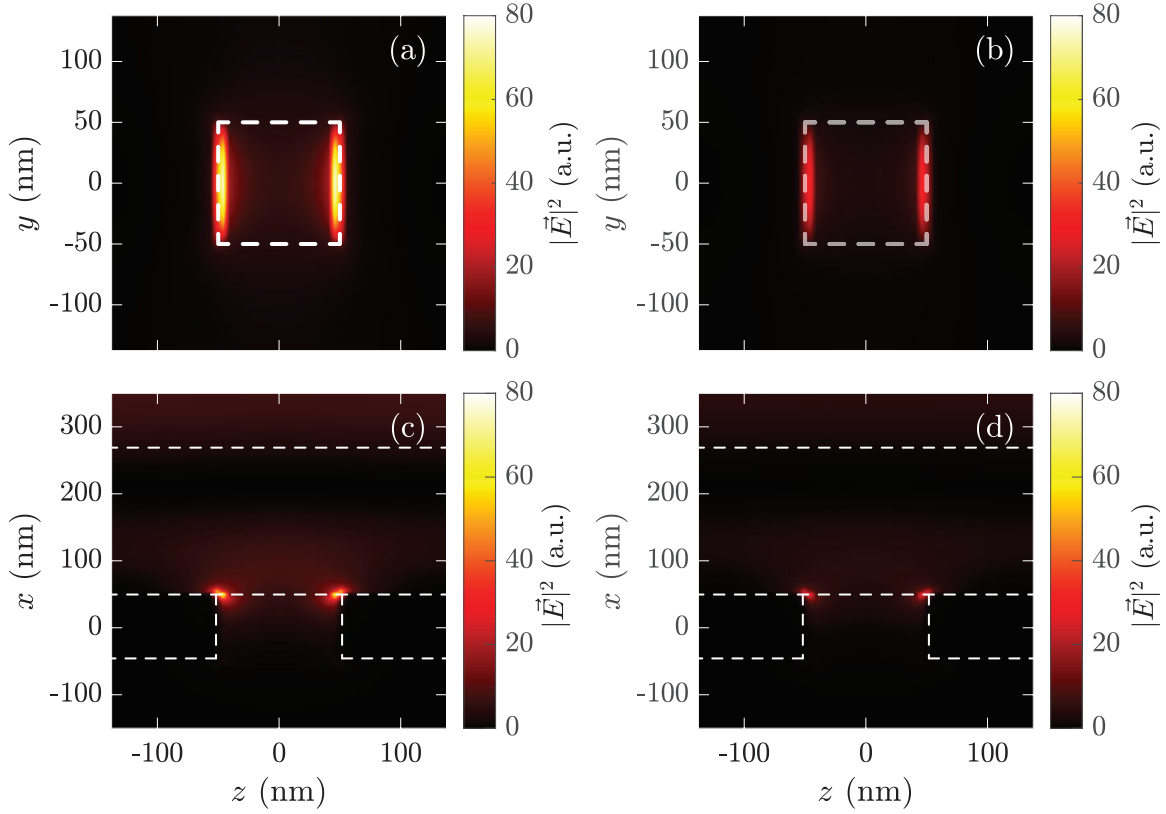
Figure 5.10: (a)-(b): The transverse section (TS) $\vec{E}$-field intensity profile of the **asymmetric DBR pair** structure taken along the metal-gain medium interface.(c)-(d) The longitudinal section (LS) $\vec{E}$-field intensity profile of the merged lattice structure taken along the dashed line shown along $y = 0$ of the graph (a),(b). (a),(c) shorter wavelength $\left|\vec{E}\right|^2$ intensity profile at 885 nm. (b),(d) Longer wavelength $\left|\vec{E}\right|^2$ intensity profile at 865 nm.

## 5.2.3  Lasing Emission Dynamics

**Near field mode dynamics**



Figure 5.11: (a) Emission intensity spectrum for varying terminating TiO$_2$ thickness ($d_L$) and (b) The spectra for $d_L = 175$ nm and $d_L = 179$ nm. The $d_L$ widths are indicated in (a) by the white dashed lines.

The effect of varying the number of contrasting pairs, in the each of the 1D PhC is different. The first-DBR tends to just refine the existing resonant modes, and reflect the emission away from the input

side towards the output side. Thus, increasing layer number in this DBR ($N_I$) causes further amplification and narrowing of lasing modes. Spectral position of the modes remain unaffected.

**Tuning terminating** $TiO_2$ **Layer :** From the theory of OTS resonance,[76] we have observed that regulation of the terminating $TiO_2$ layer thickness basically slides the resonant wavelength, along the PBG of the 1D PhC in a linear fashion. This is similar to the effect seen in regulating the gain layer thickness as both these stacks serve similar purpose with respect to the resonator topology; except that the gain medium is responsible for causing lasing emission as well. From the results obtained, we find that on increasing terminating layer thickness, both the resonant modes seems to shift from lower wavelength to higher wavelengths in the spectrum. However, the red shift of the shorter wavelength mode is much greater than the longer wavelength mode.

**Tuning Gain Medium Thickness :** Variation in gain layer thickness of the laser also tunes the spectral position of the modes. The emission peak is seen to red shift with increasing gain layer thickness. However, for width less than about 220 nm and greater than 330 nm, we find that the spectrum shows single mode only. This happends because of the limited gain lineshape centering 870 nm and the photonic bandgap of the two DBRs. It has been shown that variation of the layer just preceding the metal NHA
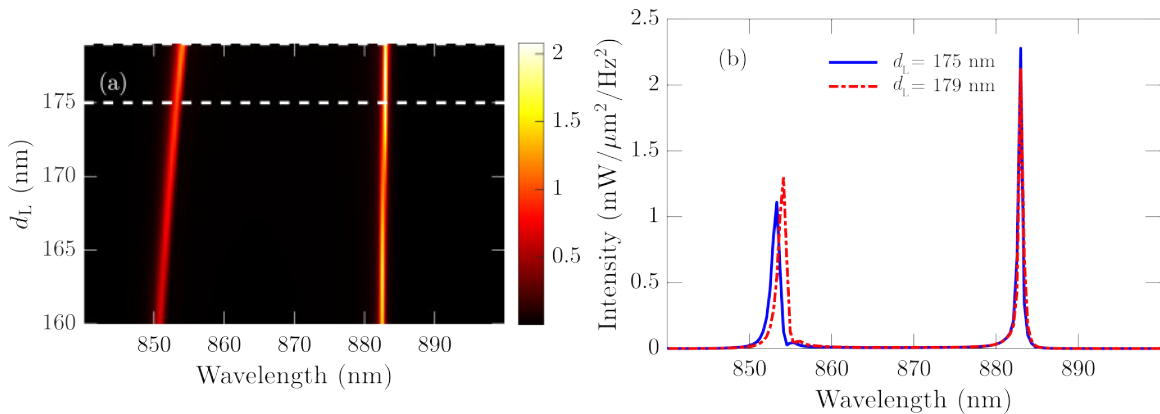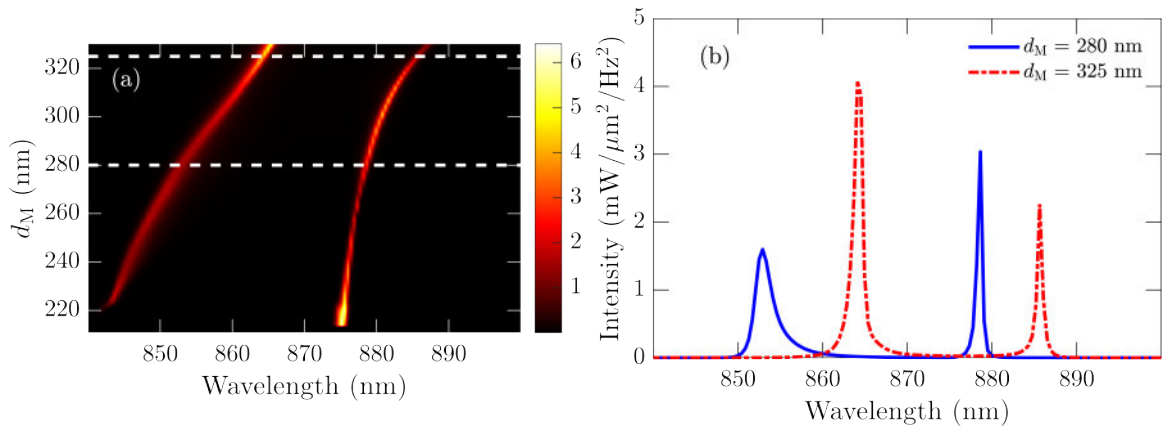
Figure 5.12: ((a) Emission intensity spectrum for varying gain medium thickness ($d_M$) and (b) The spectra for $d_M = 280$ nm and for $d_M = 325$ nm. The $d_M$ widths are indicated in (a) by the white dashed lines.

shifts the OTS resonance along the PBG. As the width is increased, the OTS resonance shifts from lower to higher wavelength, until it traverses the entire spectral bandgap in the transmission spectrum.[76] Once the OTS resonance moving in sync with the increase of layer width, passes the higher wavelength band-edge, the resonance is again seen back at the lower wavelength band-edge, except that this time the multiple OTS resonances are more closely spaced.

**Far-field Analysis**

As, already mentioned in the previous design analysis, plasmonic nano laser emits higher order modes in the spatial domain if not designed carefully. When NHA has a periodicity over the wavelength range this higher order modes tend to crop up. The difference between the wavevector of free space propagating
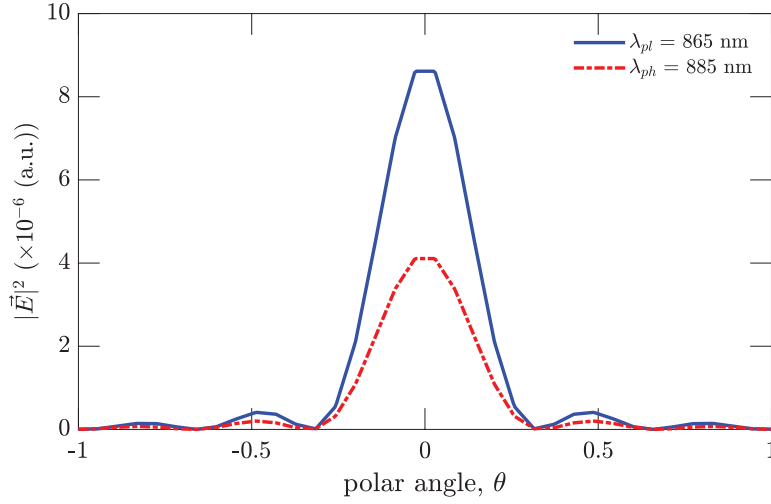
Figure 5.13: Electric field Intensity distribution on far field with respect to polar angle. at 0° azimuth.
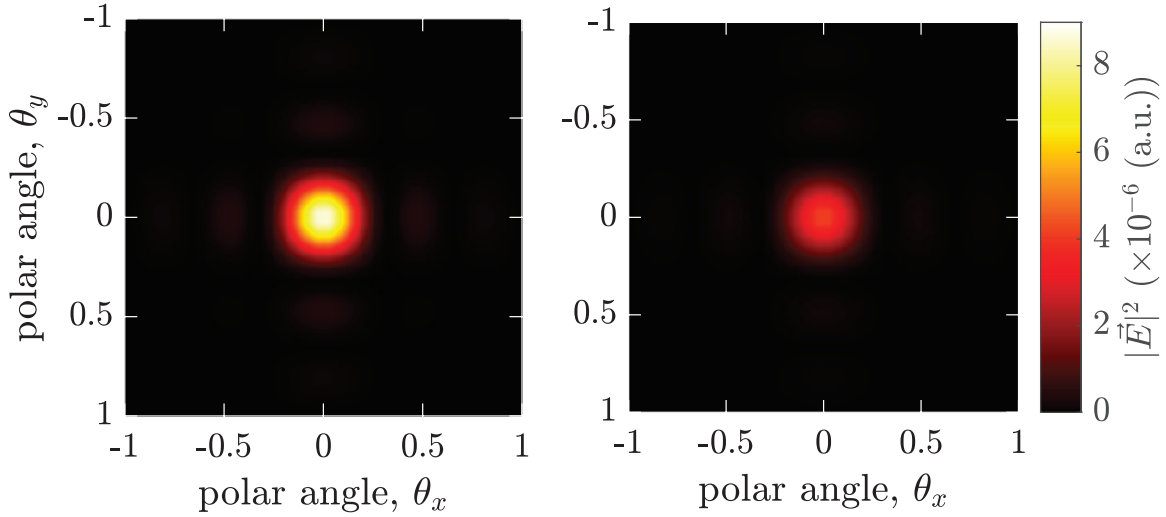


Figure 5.14: Far field emission intensity for the laser structure. Electric field intensity on a 1 m distant hemispherical surface is calculated with respect to the *x*-component and *y* component of the polar angle, *θ*. (a) Beam at 865 nm and (b) Beam at 885 nm wavelength.

modes and surface plasmon modes is the origin of generating higher order spatial modes. This can be avoided if we keep the nano-hole periodicity on the subwavelength range. Thus,as designed in the single mode plasmonic laser[3] for only emitting the zeroth order mode,we kept that in mind and saw the same effect for our dual-mode laser structures. We simulated an area of $150\mu$m$\times 150\mu$m along the *yz*-plane of the device to get the far-field performance. We did far field analysis for both of the modes separately and found similar results. The nano-holes act as resonant modes for near field calculations and as secondary point sources for the far field. These secondary sources will interfere in the far field to give rise to a interference pattern on the hemisphere, having gaussian distribution. By plotting the field intensity distribution for a range of polar angle values, it is found that far field emission intensity peak is limited to within 1° angle of the polar angle at 1m distance from the near field monitor.

# Chapter 6

# Conclusion and Future works

In this thesis, we demonstrated dual-mode emission of two plasmonic lasers. Our goal was to design an efficient multi-modal laser. At first plasmonic nanostructures were tested and tried to find the minimum device dimension beyond the diffraction limit. To address the issue of emitting higher order spatial modes of plasmonic structures, we used periodicity in subwavelength range and was successfully able to keep emission limited to zeroth order emission mode. For the design of the two main part of the laser; i.e. the gain media and cavity we went through an through investigation for material modelling, analysis and testing. All possible parameters of the design were tested and checked for possible tuning capabilities.

To carryout the thesis, we resorted to a robust Finite Difference Time Domain algorithm, in a commercial software. We modelled the gain media using four level two electron model. The model was verified to make sure that the model was working properly. To measure the extent of amplification, the transmission at lasing wavelength was plotted for varying parameters such as doping concentration and input pump. All the possible scope of enhancement were explored.

Two key phenomenon leading to energy mode formation were explored: Extraordinary Optical Transmission[69,70] (EOT) and Optical Tamm State[73,75,86] (OTS). For the design of cavity, we focused on enhancing the surface plasmon mode in the plasmonic cavity at the metal-dielectric interface. To get enhanced performance, we perforated the metal layer with nano-hole array (NHA) and incorporated Extraordinary transmission effect in the cavity. By varying hole width, thickness and periodicity we improved our understanding about NHA and EOT. We followed two different approaches to design the cavity. The first approach was the Merged Lattice NHA in metal film cavity, which has dual periodicity in the nano-hole array. The other approach was the Linear asymmetric DBR pair cavity. The lasing dynamics and mode behaviour of these structures were extensively studied. We simulated using different parameters to get the optimum response. The IR-140 dye acted as the gain medium in both structures. On top of the gain medium, the 1D photonic crystal (DBR) was cascaded. It acted as the filter for passing desired

frequencies and suppressing scattered pump on the output side. Due to dual periodicity in Merged Lattice NHA, the structure supports dual resonant OTS at metal-DBR junction. Thus by incorporating OTS and EOT of dual periodicity nano-hole array we successfully designed the cavity for our structure. This structure showed an appreciable improvement in far-field lasing performance over the structure reported by Ahmed et. al.[3]

The Linear asymmetric DBR pair laser was developed to give better tuning capacity of the plasmonic laser compared to the Merged Lattice NHA variant. It had to be done because, Merged Lattice NHA was a sensitive design. Tuning capability of the resonant modes on that structure was limited. So, we tried the other approach. We connected two DBRs in series through a spacer layer in between. After that it was terminated with simple periodic metal NHA to increase transmission and to get optical tamm state mode at metal-DBR interface. Thus cavity design was carried out successfully. Then we replaced the passive spacer layer with the gain media with IR-140 dye molecule. Pump input was given and output recorded on both transmission and receiving side. But, since only Transmission side provided useful results and were relevant, only transmission side spectra wre taken. We then proposed various ways to tune the structures to get desired wavelength emission. Far-field analysis was carried out to demonstrate that only zeroth order spatial mode was being emitted and that our designed structures has superior directional performance.

## 6.1   Future Works

Our demonstration of Linear asymmetric DBR pair dual-mode laser shows clear mode separation of almost 20 nm . It has lasing emission linewidth of almost 1nm which is remarkable for lasing emission. This can work as a superior quality coherent source with both of the mode being equally dominant. For the case of Merged lattice structure, it has showed better threshold characteristics than its single periodicity laser counterpart by reducing threshold value significantly.Not only this, the merged lattice design has reduced the divergence angle to $0.4°$ only.Both of the case has scope for improving performance farther and some issues can be dealt with. For example:

- For Merged lattice and Linear asymmetric DBR pair dual-mode lasers both structure, in the process of making it dual-mode, emission on Reflection side of the structure has increased than emission on transmission side. This can be addressed by increasing layer number of DBR but then it needs to sacrifice better threshold performance. There is scope for improvement on this area.

- None of the structure we presented are resonant on the pumping frequency. By designing additional resonant modes through optical tamm state or any other mechanism, it is possible to make it resonant also on pumping frequency. This was beyond scope of our thesis.

- Merged lattice structure is very sensitive with respect to tuning performance. It has the best threshold characteristics among it's counterparts single mode laser and Linear asymmetric DBR pair laser but the least for tuning capability for the mentioned procedure in this thesis. It can be engineered or looked further to get better tuning performance.

# Bibliography

[1]   S.-H. Chang and A. Taflove, "Finite-difference time-domain model of lasing action in a four-level two-electron atomic system," Optics express, vol. 12, no. 16, pp. 3827–3833, 2004.

[2]   S. A. Maier, Plasmonics: fundamentals and applications. Springer Science & Business Media, 2007.

[3]   Z. Ahmed and M. A. Talukder, "An efficient and directional optical tamm state assisted plasmonic nanolaser with broad tuning range," Journal of Physics Communications, vol. 2, no. 4, p. 045016, 2018.

[4]   C. H. Townes, How the Laser Happened - Adventures of a Scientist. 198 Madison Avenue, New York, New York-10016: Oxford University Press, 1999.

[5]   C. Raman and K. Krishnan, "The negative absorption of radiation," Nature, vol. 122, no. 3062, pp. 12–13, 1928.

[6]   H. A. Kramers, "The law of dispersion and bohr's theory of spectra," Nature, vol. 113, no. 2845, pp. 673–674, 1924.

[7]   H. Kopfermann and R. Ladenburg, "Experimental proof of 'negative dispersion.'," Nature, vol. 122, no. 3073, pp. 438–439, 1928.

[8]   A. Einstein, "Zur Quantentheorie der Strahlung," Physikalische Zeitschrift, vol. 18, pp. 121–128, Jan. 1917.

[9]   J. P. Gordon, H. J. Zeiger, and C. H. Townes, "The maser—new type of microwave amplifier, frequency standard, and spectrometer," Physical review, vol. 99, no. 4, p. 1264, 1955.

[10]  R. Gaulton, F. Danson, F. Ramirez, and O. Gunawan, "The potential of dual-wavelength laser scanning for estimating vegetation moisture content," Remote Sensing of Environment, vol. 132, pp. 32–39, 2013.

[11]  G. David, A. Miffre, B. Thomas, and P. Rairoux, "Sensitive and accurate dual-wavelength uv-vis polarization detector for optical remote sensing of tropospheric aerosols," Applied Physics B, vol. 108, no. 1, pp. 197–216, 2012.

[12] K. Meiners-Hagen, R. Schödel, F. Pollinger, and A. Abou-Zeid, "Multi-wavelength interferometry for length measurements using diode lasers," Measurement science review, vol. 9, no. 1, pp. 16–26, 2009.

[13] R. Dändliker, R. Thalmann, and D. Prongué, "Two-wavelength laser interferometry using super-heterodyne detection," Optics letters, vol. 13, no. 5, pp. 339–341, 1988.

[14] I. Park, C. Sydlo, I. Fischer, W. Elsäßer, and H. Hartnagel, "Generation and spectroscopic application of tunable continuous-wave terahertz radiation using a dual-mode semiconductor laser," Measurement Science and Technology, vol. 19, no. 6, p. 065305, 2008.

[15] Y. Liu, Q. Tang, L. Zhang, X. La, L. Zhao, W. Wang, and S. Liang, "Dual-wavelength dbr laser integrated with high-speed eam for thz communications," Optics express, vol. 28, no. 7, pp. 10542–10551, 2020.

[16] N. Pleros, E. E. Kriezis, and K. Vyrsokinos, "Optical interconnects using plasmonics and si-photonics," IEEE Photonics Journal, vol. 3, no. 2, pp. 296–301, 2011.

[17] A. Christ, S. Tikhodeev, N. Gippius, J. Kuhl, and H. Giessen, "Waveguide-plasmon polaritons: strong coupling of photonic and electronic resonances in a metallic photonic crystal slab," Physical review letters, vol. 91, no. 18, p. 183901, 2003.

[18] M. Stucchi, S. Cosemans, J. Van Campenhout, Z. Tőkei, and G. Beyer, "On-chip optical interconnects versus electrical interconnects for high-performance applications," Microelectronic engineering, vol. 112, pp. 84–91, 2013.

[19] D. Ozcelik, J. W. Parks, T. A. Wall, M. A. Stott, H. Cai, J. W. Parks, A. R. Hawkins, and H. Schmidt, "Optofluidic wavelength division multiplexing for single-virus detection," Proceedings of the National Academy of Sciences, vol. 112, no. 42, pp. 12933–12937, 2015.

[20] K. Ohashi, K. Nishi, T. Shimizu, M. Nakada, J. Fujikata, J. Ushida, S. Torii, K. Nose, M. Mizuno, H. Yukawa, et al., "On-chip optical interconnect," Proceedings of the IEEE, vol. 97, no. 7, pp. 1186–1198, 2009.

[21] K. Koo and A. Kersey, "Bragg grating-based laser sensors systems with interferometric interrogation and wavelength division multiplexing," Journal of Lightwave Technology, vol. 13, no. 7, pp. 1243–1249, 1995.

[22] D. K. Gramotnev and S. I. Bozhevolnyi, "Plasmonics beyond the diffraction limit," Nature photonics, vol. 4, no. 2, pp. 83–91, 2010.

[23] E. Ozbay, "Plasmonics: merging photonics and electronics at nanoscale dimensions," science, vol. 311, no. 5758, pp. 189–193, 2006.

[24] L. Novotny and S. J. Stranick, "Near-field optical microscopy and spectroscopy with pointed probes," Annu. Rev. Phys. Chem., vol. 57, pp. 303–331, 2006.

[25] T. W. Johnson, Z. J. Lapin, R. Beams, N. C. Lindquist, S. G. Rodrigo, L. Novotny, and S.-H. Oh, "Highly reproducible near-field optical imaging with sub-20-nm resolution based on template-stripped gold pyramids," <u>ACS nano</u>, vol. 6, no. 10, pp. 9168–9174, 2012.

[26] L. Novotny and B. Hecht, <u>Principles of nano-optics</u>. Cambridge university press, 2012.

[27] M. I. Stockman, "Nanoplasmonic sensing and detection," <u>Science</u>, vol. 348, no. 6232, pp. 287–288, 2015.

[28] M. I. Stockman, K. Kneipp, S. I. Bozhevolnyi, S. Saha, A. Dutta, J. Ndukaife, N. Kinsey, H. Reddy, U. Guler, V. M. Shalaev, <u>et al.</u>, "Roadmap on plasmonics," <u>Journal of Optics</u>, vol. 20, no. 4, p. 043001, 2018.

[29] J. A. Schuller, E. S. Barnard, W. Cai, Y. C. Jun, J. S. White, and M. L. Brongersma, "Plasmonics for extreme light concentration and manipulation," <u>Nature materials</u>, vol. 9, no. 3, pp. 193–204, 2010.

[30] R.-M. Ma and R. F. Oulton, "Applications of nanolasers," <u>Nature Nanotechnology</u>, vol. 14, no. 1, pp. 12–22, 2019.

[31] M. Stockman, "Spasers to speed up cmos processors," tech. rep., Georgia State University Research Foundation, Atlanta, GA (United States), 2018.

[32] Z. Xie, W. Yu, T. Wang, H. Zhang, Y. Fu, H. Liu, F. Li, Z. Lu, and Q. Sun, "Plasmonic nanolithography: a review," <u>Plasmonics</u>, vol. 6, no. 3, p. 565, 2011.

[33] M. Fedoruk, M. Meixner, S. Carretero-Palacios, T. Lohmuller, and J. Feldmann, "Nanolithography by plasmonic heating and optical manipulation of gold nanoparticles," <u>ACS nano</u>, vol. 7, no. 9, pp. 7648–7653, 2013.

[34] W. Srituravanich, N. Fang, C. Sun, Q. Luo, and X. Zhang, "Plasmonic nanolithography," <u>Nano letters</u>, vol. 4, no. 6, pp. 1085–1088, 2004.

[35] S. Kawata, Y. Inouye, and P. Verma, "Plasmonics for near-field nano-imaging and superlensing," <u>Nature photonics</u>, vol. 3, no. 7, pp. 388–394, 2009.

[36] J. N. Anker, W. P. Hall, O. Lyandres, N. C. Shah, J. Zhao, and R. P. Van Duyne, "Biosensing with plasmonic nanosensors," in <u>Nanoscience and Technology: A Collection of Reviews from Nature Journals</u>, pp. 308–319, World Scientific, 2010.

[37] J. Homola, "Surface plasmon resonance sensors for detection of chemical and biological species," <u>Chemical reviews</u>, vol. 108, no. 2, pp. 462–493, 2008.

[38] G. Conibeer, "Third-generation photovoltaics," <u>Materials today</u>, vol. 10, no. 11, pp. 42–50, 2007.

[39] R. F. Oulton, V. J. Sorger, T. Zentgraf, R.-M. Ma, C. Gladden, L. Dai, G. Bartal, and X. Zhang, "Plasmon lasers at deep subwavelength scale," <u>Nature</u>, vol. 461, no. 7264, pp. 629–632, 2009.

[40] R. S. Savelev, A. P. Slobozhanyuk, A. E. Miroshnichenko, Y. S. Kivshar, and P. A. Belov, "Sub-wavelength waveguides composed of dielectric nanoparticles," Physical Review B, vol. 89, no. 3, p. 035435, 2014.

[41] B. Afinogenov, V. Bessonov, A. Nikulin, and A. Fedyanin, "Observation of hybrid state of tamm and surface plasmon-polaritons in one-dimensional photonic crystals," Applied Physics Letters, vol. 103, no. 6, p. 061112, 2013.

[42] W. L. Barnes, A. Dereux, and T. W. Ebbesen, "Surface plasmon subwavelength optics," nature, vol. 424, no. 6950, pp. 824–830, 2003.

[43] R. H. Ritchie, "Plasma losses by fast electrons in thin films," Physical review, vol. 106, no. 5, p. 874, 1957.

[44] A. V. Zayats, I. I. Smolyaninov, and A. A. Maradudin, "Nano-optics of surface plasmon polaritons," Physics reports, vol. 408, no. 3-4, pp. 131–314, 2005.

[45] K. L. Kelly, E. Coronado, L. L. Zhao, and G. C. Schatz, "The Optical Properties of Metal Nanoparticles: The Influence of Size, Shape, and Dielectric Environment," The Journal of Physical Chemistry B, vol. 107, no. 3, pp. 668–677, 2003.

[46] K. G. Stamplecoskie and J. C. Scaiano, "Light emitting diode irradiation can control the morphology and optical properties of silver nanoparticles," Journal of the American Chemical Society, vol. 132, no. 6, pp. 1825–1827, 2010.

[47] G. A. Wurtz, J. S. Im, S. K. Gray, and G. P. Wiederrecht, "Optical scattering from isolated metal nanoparticles and arrays," The Journal of Physical Chemistry B, vol. 107, no. 51, pp. 14191–14198, 2003.

[48] K.-H. Su, Q.-H. Wei, X. Zhang, J. Mock, D. R. Smith, and S. Schultz, "Interparticle coupling effects on plasmon resonances of nanogold particles," Nano letters, vol. 3, no. 8, pp. 1087–1090, 2003.

[49] S. A. Maier, P. G. Kik, and H. A. Atwater, "Observation of coupled plasmon-polariton modes in au nanoparticle chain waveguides of different lengths: Estimation of waveguide loss," Applied Physics Letters, vol. 81, no. 9, pp. 1714–1716, 2002.

[50] N. Lawandy, "Localized surface plasmon singularities in amplifying media," Applied physics letters, vol. 85, no. 21, pp. 5040–5042, 2004.

[51] D. Wang, A. Yang, W. Wang, Y. Hua, R. D. Schaller, G. C. Schatz, and T. W. Odom, "Band-edge engineering for controlled multi-modal nanolasing in plasmonic superlattices," Nature nanotechnology, vol. 12, no. 9, p. 889, 2017.

[52] S. Pourjamal, T. K. Hakala, M. Nečada, F. Freire-Fernández, M. Kataja, H. Rekola, J.-P. Martikainen, P. Törmä, and S. van Dijken, "Lasing in ni nanodisk arrays," ACS nano, vol. 13, no. 5, pp. 5686–5692, 2019.

[53] J. M. Winkler, M. J. Ruckriegel, H. Rojo, R. C. Keitel, E. De Leo, F. T. Rabouw, and D. J. Norris, "Dual-wavelength lasing in quantum-dot plasmonic lattice lasers," <u>ACS nano</u>, vol. 14, no. 5, pp. 5223–5232, 2020.

[54] A. Taflove and S. C. Hagness, <u>Computational electrodynamics: the finite-difference time-domain method</u>. Artech house, 2005.

[55] I. . Lumerical, <u>Finite Difference Time Domain (FDTD) solver introduction</u>, 2020 (accessed June 29, 2020). `https://support.lumerical.com/hc/en-us/articles/360034914633-Finite-Difference-Time-Domain-FDTD-solver-introduction`.

[56] K. Yee, "Numerical solution of initial boundary value problems involving maxwell's equations in isotropic media," <u>IEEE Transactions on antennas and propagation</u>, vol. 14, no. 3, pp. 302–307, 1966.

[57] M. Dridi and G. C. Schatz, "Model for describing plasmon-enhanced lasers that combines rate equations with finite-difference time-domain," <u>Josa B</u>, vol. 30, no. 11, pp. 2791–2797, 2013.

[58] W. Zhou, M. Dridi, J. Y. Suh, C. H. Kim, D. T. Co, M. R. Wasielewski, G. C. Schatz, T. W. Odom, et al., "Lasing action in strongly coupled plasmonic nanocavity arrays," <u>Nature nanotechnology</u>, vol. 8, no. 7, p. 506, 2013.

[59] H. Yokoyama and S. Brorson, "Rate equation analysis of microcavity lasers," <u>Journal of Applied Physics</u>, vol. 66, no. 10, pp. 4801–4805, 1989.

[60] G. Björk, A. Karlsson, and Y. Yamamoto, "Definition of a laser threshold," <u>Physical Review A</u>, vol. 50, no. 2, p. 1675, 1994.

[61] H. W. Siesler, Y. Ozaki, S. Kawata, and H. M. Heise, <u>Near-infrared spectroscopy: principles, instruments, applications</u>. John Wiley & Sons, 2008.

[62] H. Caglayan, S.-H. Hong, B. Edwards, C. R. Kagan, and N. Engheta, "Near-infrared metatronic nanocircuits by design," <u>Physical review letters</u>, vol. 111, no. 7, p. 073904, 2013.

[63] A. Yang, T. B. Hoang, M. Dridi, C. Deeb, M. H. Mikkelsen, G. C. Schatz, and T. W. Odom, "Real-time tunable lasing from plasmonic nanocavity arrays," <u>Nature communications</u>, vol. 6, no. 1, pp. 1–7, 2015.

[64] F. Lytle, R. Parrish, and W. Barnes, "An introduction to time-resolved pump/probe spectroscopy," <u>Applied spectroscopy</u>, vol. 39, no. 3, pp. 444–451, 1985.

[65] S. Popov, "Dye photodestruction in a solid-state dye laser with a polymeric gain medium," <u>Applied optics</u>, vol. 37, no. 27, pp. 6449–6455, 1998.

[66] S. Singh, V. Kanetkar, G. Sridhar, V. Muthuswamy, and K. Raja, "Solid-state polymeric dye lasers," <u>Journal of Luminescence</u>, vol. 101, no. 4, pp. 285–291, 2003.

[67] H. A. Bethe, "Theory of diffraction by small holes," <u>Physical review</u>, vol. 66, no. 7-8, p. 163, 1944.

[68] C. J. Bouwkamp, "Diffraction theory," Reports on progress in physics, vol. 17, no. 1, p. 35, 1954.

[69] T. W. Ebbesen, H. J. Lezec, H. Ghaemi, T. Thio, and P. A. Wolff, "Extraordinary optical transmission through sub-wavelength hole arrays," Nature, vol. 391, no. 6668, pp. 667–669, 1998.

[70] H. Liu and P. Lalanne, "Microscopic theory of the extraordinary optical transmission," Nature, vol. 452, no. 7188, pp. 728–731, 2008.

[71] K. K. Koerkamp, S. Enoch, F. B. Segerink, N. Van Hulst, and L. Kuipers, "Strong influence of hole shape on extraordinary transmission through periodic arrays of subwavelength holes," Physical review letters, vol. 92, no. 18, p. 183901, 2004.

[72] K. Van der Molen, K. K. Koerkamp, S. Enoch, F. B. Segerink, N. Van Hulst, and L. Kuipers, "Role of shape and localized resonances in extraordinary transmission through periodic arrays of subwavelength holes: Experiment and theory," Physical Review B, vol. 72, no. 4, p. 045421, 2005.

[73] M. Kaliteevski, I. Iorsh, S. Brand, R. Abram, J. Chamberlain, A. Kavokin, and I. Shelykh, "Tamm plasmon-polaritons: Possible electromagnetic states at the interface of a metal and a dielectric bragg mirror," Physical Review B, vol. 76, no. 16, p. 165415, 2007.

[74] I. Tamm, "A possible binding of the electrons on a crystal surface," Zh. Eksp. Teor. Fiz, vol. 3, pp. 34–35, 1933.

[75] M. Lopez-Garcia, Y.-L. Ho, M. Taverne, L.-F. Chen, M. Murshidy, A. Edwards, M. Serry, A. Adawi, J. Rarity, and R. Oulton, "Efficient out-coupling and beaming of tamm optical states via surface plasmon polariton excitation," Applied physics letters, vol. 104, no. 23, p. 231116, 2014.

[76] H. Zhou, G. Yang, K. Wang, H. Long, and P. Lu, "Multiple optical tamm states at a metal–dielectric mirror interface," Optics letters, vol. 35, no. 24, pp. 4112–4114, 2010.

[77] X. Shou, A. Agrawal, and A. Nahata, "Role of metal film thickness on the enhanced transmission properties of a periodic array of subwavelength apertures," Optics express, vol. 13, no. 24, pp. 9834–9840, 2005.

[78] G. Alagappan and C. Png, "Localization of waves in merged lattices," Scientific Reports, vol. 6, p. 31620, 2016.

[79] X. Zhang, G. Liu, Z. Liu, Z. Cai, Y. Hu, X. Liu, G. Fu, H. Gao, and S. Huang, "Effects of compound rectangular subwavelength hole arrays on enhancing optical transmission," IEEE Photonics Journal, vol. 7, no. 1, p. 1–8, 2015.

[80] P. W. Anderson, "Absence of diffusion in certain random lattices," Physical review, vol. 109, no. 5, p. 1492, 1958.

[81] J. Liu, P. Garcia, S. Ek, N. Gregersen, T. Suhr, M. Schubert, J. Mørk, S. Stobbe, and P. Lodahl, "Random nanolasing in the anderson localized regime," Nature Nanotechnology, vol. 9, no. 4, pp. 285–289, 2014.

[82] R. Brückner, M. Sudzius, S. I. Hintschich, H. Fröb, V. G. Lyssenko, and K. Leo, "Hybrid optical tamm states in a planar dielectric microcavity," Physical Review B, vol. 83, no. 3, p. 033405, 2011.

[83] G. Pandey, A. K. Shukla, K. B. Thapa, and J. Pandey, "Enhanced of photonic bandgaps in one-dimensional plasma photonic crystal with defect," in Advances in Optical Science and Engineering, pp. 219–225, Springer, 2017.

[84] Z. Azad, M. S. Islam, and M. A. Talukder, "Mode-resolved analysis of a planar multi-layer plasmonic nanolaser," Optics Communications, vol. 482, p. 126614.

[85] I. V. Treshin, V. V. Klimov, P. N. Melentiev, and V. I. Balykin, "Optical tamm state and extraordinary light transmission through a nanoaperture," Physical Review A, vol. 88, no. 2, p. 023832, 2013.

[86] M. Sasin, R. Seisyan, M. Kalitteevski, S. Brand, R. Abram, J. Chamberlain, A. Y. Egorov, A. Vasil'Ev, V. Mikhrin, and A. Kavokin, "Tamm plasmon polaritons: Slow and spatially compact light," Applied physics letters, vol. 92, no. 25, p. 251112, 2008.